

Design and Validation of a Powered Knee–Ankle Prosthesis With High-Torque, Low-Impedance Actuators

Toby Elery , *Student Member, IEEE*, Siavash Rezaadeh , *Member, IEEE*, Christopher Nesler, and Robert D. Gregg , *Senior Member, IEEE*

Abstract—In this article, we present the design of a powered knee–ankle prosthetic leg, which implements high-torque actuators with low-reduction transmissions. The transmission coupled with a high-torque and low-speed motor creates an actuator with low mechanical impedance and high backdrivability. This style of actuation presents several possible benefits over modern actuation styles in emerging robotic prosthetic legs, which include free-swinging knee motion, compliance with the ground, negligible unmodeled actuator dynamics, less acoustic noise, and power regeneration. Benchmark tests establish that both joints can be backdriven by small torques ($\sim 1\text{--}3\text{ N}\cdot\text{m}$) and confirm the small reflected inertia. Impedance control tests prove that the intrinsic impedance and unmodeled dynamics of the actuator are sufficiently small to control joint impedance without torque feedback or lengthy tuning trials. Walking experiments validate performance under the designed loading conditions with minimal tuning. Finally, the regenerative abilities, low friction, and small reflected inertia of the presented actuators reduced power consumption and acoustic noise compared to state-of-the-art powered legs.

Index Terms—Actuator design, backdrivability, powered prostheses, rehabilitation robotics.

Manuscript received November 8, 2019; revised April 3, 2020; accepted June 21, 2020. Date of publication July 13, 2020; date of current version December 3, 2020. This work was supported by the National Institute of Child Health & Human Development of the NIH under Award Number DP2HD080349 and R01HD094772. This work was also supported by NSF Award 1637704/1854898. The content is solely the responsibility of the authors and does not necessarily represent the official views of the NIH or the NSF. Robert D. Gregg, IV, Ph.D., holds a Career Award at the Scientific Interface from the Burroughs Wellcome Fund. This article was recommended for publication by Associate Editor H. Vallery and Editor E. Yoshida upon evaluation of the reviewers' comments. (*Corresponding author: Robert Gregg.*)

Toby Elery is with the Departments of Bioengineering and Mechanical Engineering, The University of Texas at Dallas, Richardson, TX 75080 USA (e-mail: toby.elery@utdallas.edu).

Siavash Rezaadeh is with the Department of Mechanical Engineering, University of Denver, Denver, CO 80208 USA (e-mail: s.rezaadeh@gmail.com).

Christopher Nesler and Robert D. Gregg are with the Department of Electrical Engineering and Computer Science, Robotics Institute, University of Michigan, Ann Arbor, MI 48109 USA (e-mail: neslerc@umich.edu; rdgregg@umich.edu).

This article has supplementary downloadable material available at <https://ieeexplore.ieee.org>, provided by the authors. The material consists of a video, demonstrating a visual presentation of the newly designed knee–ankle prosthetic leg, and how its validation tests were performed. The video includes backdrive, free-swing knee, closed-loop position control, and open-loop impedance control benchtop experiments, and also includes walking experiments with both an able-bodied and amputee subject. The size of the video is 38.6 MB. Contact toby.elery@utdallas.edu for further questions about this work.

Color versions of one or more of the figures in this article are available online at <https://ieeexplore.ieee.org>.

Digital Object Identifier 10.1109/TRO.2020.3005533

I. INTRODUCTION

USE of conventional passive prostheses after lower limb loss results in gait that is slower, less stable, and less energy efficient than able-bodied (AB) locomotion [1], [2]. Passive prostheses aim to alleviate the effects of amputation using mechanisms, such as springs, cams, and dampers to mimic normative gait patterns. However, passive prostheses are limited in functionality due to the fact that such mechanisms can only dissipate energy that the user introduces. Although these passive devices restore some functionality, amputees are typically left with an asymmetric gait [3]. Moreover, most devices are designed for level-ground walking conditions and do not adequately facilitate tasks, such as sit-to-stand or stair ascent/descent. Semiactive prostheses, such as the Ottobock C-Leg, utilize microprocessors to control the damping of joints via small actuators that manipulate hydraulic valves during the user's gait [4], [5]. This approach allows for a single product to be easily adaptable to a variety of subjects, environments, and tasks, but semiactive devices can still only dissipate energy from the user's gait. Powered prostheses can actively inject energy and, therefore, have greater capability to restore mobility and quality of life to those who live with the loss of a limb.

In the last decade, a great amount of research has gone into the design and control of powered prosthetic (PR) limbs, resulting in several PR devices that implement a variety of actuation schemes [6]–[9]. Rigid, or nonbackdrivable actuators, that implement transmissions, such as worm gears [10] or cam-follower/leadscrews [11], have recently been implemented in order to reduce the size and weight of the prosthesis. Several other PR legs implement actuators with low backdrivability, or high impedance. Such actuators commonly include high-speed, low-torque motors with high-ratio transmissions, such as ball screws or multiple/belt gear stages [4], [6], [12]–[24]. This high-impedance actuation scheme, which typically consists of reduction ratios greater than 100:1, results in more rigid joints and large reflected inertias. This can cause more painful impact forces on the residual limb after extended use. This also forces the knee swing to be actively controlled rather than naturally free-swinging (such as, for example, the C-Leg), which results in higher energy consumption and reduced battery life. Additionally, more meshing or rolling parts in the transmission result in more acoustic noise that is bothersome to patients. A

recently developed PR leg implements a transmission with a reduced reduction ratio of $\sim 50:1$ [25], but the resulting actuator impedance is still high enough to share some of the limitations discussed earlier.

In the past few years, legged robots, such as the quadruped MIT Cheetah [26], biped Cassie [27], and others [28]–[32], have embraced high-torque motors with low ratio or no transmissions. High-torque, low-reduction-ratio actuators (also referred to as low-impedance actuators) offer several benefits for legged robotics that are also desirable in powered prostheses. The lower mechanical impedance (inertias and frictional losses) of these actuators minimizes the effect of unmodeled dynamics, which in turn simplifies an otherwise complex control problem, increases robustness, and makes the system behave closer to an ideal model. Force control in these actuators can be comparable to series elastic actuators (SEAs) without their design and manufacturing complexities and low bandwidth [17], [33]. Low-impedance actuators are also compliant, which aids in regenerating energy and mitigating impact forces [34].

We propose that low-impedance actuators also have benefits specific to powered prostheses, including passive knee-swing motion, energy sharing between joints, acoustic sound reduction, and compliance with the ground through impedance control. A free-swinging knee joint allows for a more natural gait while reducing the power requirements of the actuator during swing phase. Energy sharing phases of gait, such as mid-stance, where the ankle regenerates energy while the knee demands it, can lead to longer periods of untethered operation, which is critical for robotic legs in consumer applications. The low mechanical impedance from reduced friction and gear meshings can lead to a quieter device, which is crucial for the clinical acceptance of powered PR legs. Finally, the implementation of biological joint impedances can promote natural compliance with the ground and provide smoother touchdown impacts, which can in turn improve efficiency of the system and comfort for the user. Although there have been attempts to control prosthesis joints using open-loop torque control [18], the nonnegligible dynamics of the actuator would considerably affect the joint torque and, thus, requiring lengthy sessions of tuning impedance parameters [35].

In the process of designing low-impedance actuators, transmission design is a critical problem. Single-stage planetary transmissions are extremely efficient and have less intrinsic impedance than multistage transmissions, but are typically limited to ratios below 10:1. Therefore, efficient single-stage transmissions usually require a customized motor design, such as Seok *et al.* [26], to achieve the high output torques required during legged locomotion. Other transmission choices used in robotic legs, such as harmonic and cycloid gear drives, exhibit other problems, such as efficiency and manufacturing complexities, respectively [36]. To overcome these shortcomings, we propose using a single-stage stepped-planet compound planetary gear transmission (SPC-PGT) [37] coupled with a high torque-density motor. As we will show, the resulting actuator has low mechanical impedance and high backdrivability. Although this style of transmission has the same number of gears meshing as a single-stage planetary transmission, it offers a higher

range of reduction ratios while maintaining high efficiency and low acoustic sound. The manufacturability of this transmission style is also simplified compared to previously mentioned styles.

This article extends the benchtop validation of the powered transfemoral (TF) PR leg presented in [38] through the implementation of a walking controller that utilizes the compliant nature of the leg's actuators to facilitate smooth and easy switching between impedance and position control paradigms at different walking speeds. Moreover, the low impedance of the actuators allows for the direct use of estimated human joint impedance. This can simplify the implementation and tuning of the biomimetic walking controller compared to typical open-loop (no joint torque feedback) impedance control of actuators with nonnegligible intrinsic impedance. Examining the leg during walking allows for the quantification of specific properties not measurable during benchtop testing, such as kinematics and kinetics, electrical power, and acoustic sound levels during normative loading conditions. We validate the actuator design in walking experiments with an AB subject, demonstrating normative kinematics and pushoff power with reduced acoustic noise compared to previous designs. These tests also demonstrate that accurate impedance and torque control can be achieved without torque sensors. These sensors are removed in a revised assembly to minimize weight and volume for experiments with a TF amputee subject. In these trials, the joint compliance facilitates energy regeneration and sharing between joints during periods of negative work, such as knee swing extension. This is useful to increase the efficiency of powered prostheses, which leads to extended battery life and usage time [9].

The mechatronic design of the powered PR leg is presented in Section II, including the motor, transmission, electrical system, and structure of both joints. Section III introduces the leg's control method implemented in Section IV. Section IV-A presents a series of benchtop experiments that characterize the velocity, torque, position tracking, and backdrive capabilities of the actuators. Section IV-B presents the setup and results of walking experiments, including power regeneration and acoustic sound reduction during walking at different speeds. Section V discusses the results. Finally, Section VI concludes this article.

II. HARDWARE DESIGN

A. Design Overview

The main objective of this prosthesis design is to achieve humanlike joint impedance and dynamics, such that biological joint impedance values can be directly implemented into joint-level control. To achieve this, the design must have negligible intrinsic joint inertia similar to human joints [39]. Therefore, our main design goal is to minimize the reflected inertia of the joint's actuator while preserving the required torque capabilities. For reference, we aim for a substantially reduced actuator inertia compared to that of the state-of-the-art powered prosthesis (third generation Vanderbilt leg—knee actuator; $0.1032 \text{ kg}\cdot\text{m}^2$) [16]. Additionally, each actuator must be able to meet the necessary torque, velocity, position, and power requirements for level ground, stair ascent, and stair descent ambulation [39], [40],

TABLE I
KNEE AND ANKLE REQUIREMENTS FOR A 75-KG SUBJECT

	Ankle Requirements	Knee Requirements
Peak Torque	~130 Nm	~120 Nm
Velocity	360°/s	330°/s
Position	-28° to 20°	0° to 105°
Peak Power	345 W	220 W

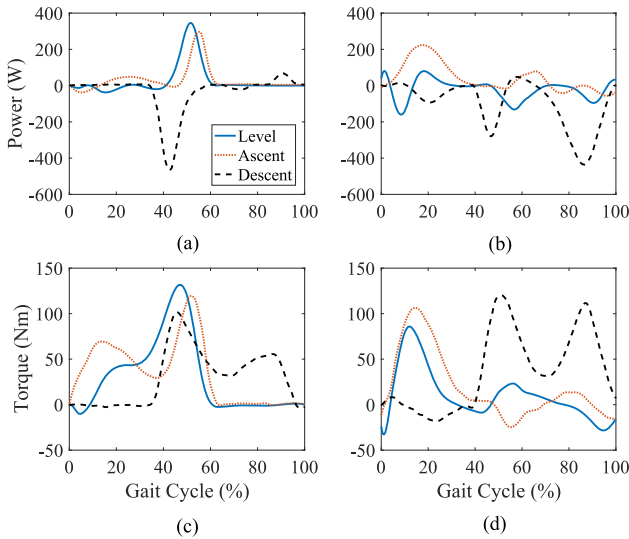


Fig. 1. (a) and (c) Ankle and (b) and (d) knee average joint powers and torques for healthy individuals (75 kg) [39], used for defining peak requirements of the powered prosthesis. Solid blue lines indicate level ground walking at fast speeds, where dotted red lines and dashed black lines represent stair ascent and descent, respectively.

as shown in Table I. Fig. 1 presents the required joint power and torque throughout the gait cycle for these tasks. We wish to exceed the peak torque and power capabilities of state-of-the-art PR legs to fully match biological levels for heavier subjects and more demanding tasks, such as fast walking and stair ascent, which require ~130 N·m and ~350 W for a 75-kg individual. Note that the Vanderbilt leg is still capable of navigating stairs with a peak power of 200 W [41], [42]. Finally, a self-imposed requirement of an adjustable shank length allows for a larger population of potential users.

Structural components of both actuators were optimized using the finite element analysis software, ANSYS, to ensure structural integrity for loading conditions of a 113.4-kg (250 lbs) user and against impacts (~3 times the subject weight) during level ground walking and stair ambulation. Most machined components were made of 7075-T6 aluminum, with a few shafts, gears, and bearings made of stainless steel. The leg was assembled in two iterations (see Fig. 2): a preliminary one with torque sensors to validate the actuator capabilities during benchtop and AB experiments, and a final one without torque sensors to reduce size and mass for amputee testing. The first assembly (see Fig. 2, left-hand side) weighs approximately 6.05 kg without batteries or 6.61 kg with batteries. A weight breakdown is shown in Table II under “Preliminary Mass.” The leg’s lithium-polymer batteries, TP1600-4SA80X (Thunder Power, Las Vegas, NV, USA), were kept off-board for benchtop and AB experiments to

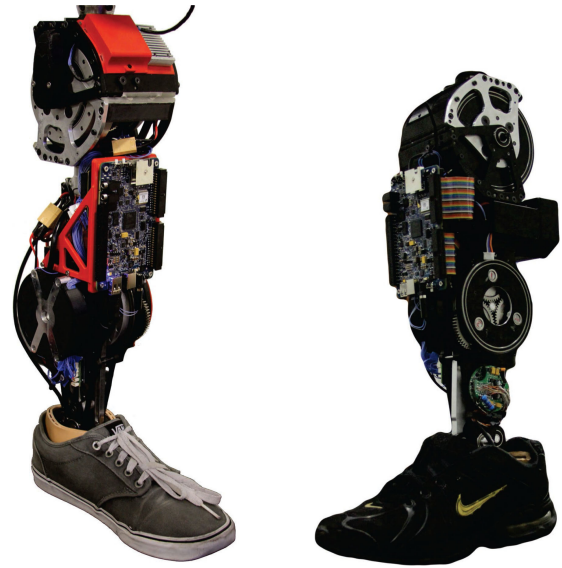


Fig. 2. Final assemblies of the PR leg. The image on the left-hand side displays the first version of the prosthesis (without batteries), which was used in benchtop and AB testing. The image on the right-hand side displays the prosthesis after revisions were made for amputee experiments (i.e., torque sensor removal and on-board batteries).

TABLE II
APPROXIMATE MASS OF LEG COMPONENTS

	Preliminary Mass (kg)	Revised Mass (kg)
Motors	1.18	1.18
Transmissions	1.39	1.32
Torque Sensors	0.38	-
Load Cell	0.19	0.19
Structure	2.29	2.17
CF Foot	0.30	0.30
Electronics	0.29	0.45
Wiring	0.03	0.05
Li-Po Batteries	0.56	0.43
Total	6.61	6.09

ensure safety due to the potential for high regenerative currents. Note that for the second assembly, batteries were mounted on-board with active voltage monitoring of each individual cell. The knee actuator is ~13.7 cm wide (medial-lateral) by 12.9 cm deep (anterior-posterior). The ankle joint is ~6.5 cm wide by 7.6 cm deep. The section corresponding to the calf is ~11.8 cm wide by ~12.9 cm deep, which equates to approximately the 30th and 50th percentile of adult male and female calf circumference, respectively [43]. Furthermore, the distance from the top of the prosthesis to the knee center is ~7.8 cm, the minimum distance between the knee and ankle center is ~32.9 cm, and the distance from the ankle center and the ground is ~8.5 cm (including the cosmetic foot shell). Finally, in an effort to reduce weight, components that are under minimal loading conditions were three-dimensional (3-D) printed in ABS plastic.

B. Revisions for Amputee Testing

The prosthesis required torque sensors in the testing and validation of its actuators during benchtop and AB walking experiments. However, the results in Sections IV-A.6 and IV-C.1

demonstrated the precise open-loop torque control capabilities of the actuators, thus rendering the torque sensors unnecessary for further experimentation. Therefore, prior to amputee experiments, revisions were made to the structure of the prosthesis to remove both the knee and ankle torque sensors, as shown on the right-hand side in Fig. 2. This is important because it led to a reduction in mass and volume of the leg, both of which are important when translating to the clinical setting. The removal of these sensors reduced the medial–lateral width of each actuator by ~ 1 cm. In addition to the removal of the torque sensors, smaller batteries (TP870-3SR70, Thunder Power) were selected to be mounted on the leg, which enabled untethered operation of the prosthesis. The mass of the entire prosthesis was reduced by ~ 0.52 kg, bringing the mass to 6.09 kg, including batteries. A breakdown of the revised mass is given in Table II.

C. Motor and Driver

High-torque motors typically used in industrial settings have large masses and volumes due to their robust housings and heat sinks. These motors are typically fixed in place, leading to minimal consideration of weight in their design. However, for implementation into a powered PR leg, it was necessary for us to select a motor with high torque density, to ensure that our actuator could produce the required torque while remaining as light and compact as possible. To this end, we selected the ILM 85 \times 26 motor kit, RoboDrive, Seefeld, Germany. This frameless, brushless dc motor kit allowed for the design of a custom housing that can withstand loading conditions and dissipate heat while reducing the weight compared to industrial motor assemblies. This motor has a manufacturer-rated torque of 2.6 N·m, peak torque of 8.3 N·m, and a maximum velocity of 1500 r/min. It is rated at 410 W, 11 A, and 48 V. A 25/100 Solo Gold Twitter motor driver (Elmo Motion Control, Petah Tikva, Israel) is used, which has a rated current of 17.6 A and a peak current of 35.2 A. The small size and mass of the driver (22.2 g) make it ideal for minimizing overall actuator size and mass.

D. Transmission

It was necessary to realize a transmission that would increase torque and decrease speed of the selected motor to fit within the desired torque/velocity range while minimizing the reduction ratio and, therefore, the reflected inertia. We determined that a reduction ratio of between 20:1 and 25:1 would be needed to achieve maximum torques while maintaining desired speeds. Therefore, we designed a custom SPC-PGT with a 22:1 reduction. Considering the peak torque of the actuators (~ 183 N·m), the Lewis factor equation for gear tooth stress was used in the initial selection of off-the-shelf gears (SDP/SI, Hicksville, NY, USA), which were then revised using finite element analysis (FEA) analysis to optimize for weight. The SPC-PGT consists of one sun gear, one ring gear, and six planet gears. Traditional planetary gear transmissions have only three planet gears, which mesh between the sun and ring gears. However, the SPC-PGT used here calls for three sun-planet gears and three ring-planet gears. Each sun-planet gear is coaxially fixed in relation to

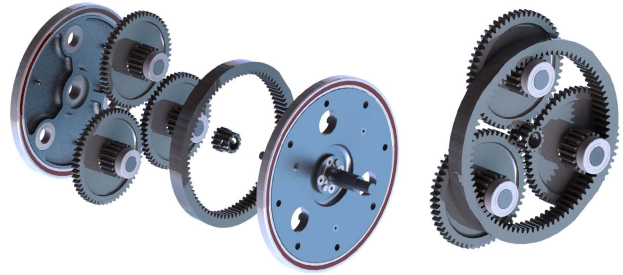


Fig. 3. CAD model of the planetary gear transmission. The image on the left-hand side illustrates an exploded view of the entire transmission (including planet carriers), whereas the image on the right-hand side demonstrates the gear layout after assembly.

its corresponding ring-planet gear through a keyed shaft. The sun-planet gears mesh with the sun gear, radially located 120° apart from each other. Similarly, the ring-planet gears are meshed with the ring gear, and are also radially located 120° apart from each other. The shafts of the planet gears are held on either side by what is commonly referred to as a planet carrier. The transmission assembly can be seen in Fig. 3.

Although planetary gear transmissions have multiple input-to-output configurations, the presented gearbox uses the sun gear as the input and the planetary carrier as the output to achieve the maximum ratio possible given a specific gear set. A traditional single-stage planetary gear transmission with the same input to output configuration has a reduction ratio found by $\tau_m/\tau_j = (D_r + D_s)/(D_s)$, whereas the reduction ratio of the single-stage SPC-PGT is found by $\tau_m/\tau_j = 1 + (D_r D_{sp})/(D_s D_{rp})$, where τ_m and τ_j are the motor and joint torque, respectively, and D_s , D_{sp} , D_{rp} , and D_r are the sun, sun-planet, ring-planet, and ring gear diameters, respectively. Due to geometric constraints of a traditional planetary gear transmission, reduction ratios are typically limited to 10:1. However, the SPC-PGT can easily achieve higher reduction ratios in approximately the same geometric volume. Although the presented design differs from a traditional single-stage planetary gear transmission, the number of gears meshed together is the exact same, thus increasing the obtainable reduction ratio without decreasing efficiency or increasing acoustic sound [44]. This also minimizes backlash, which measured less than 36 arcmin (0.6°) during walking. Values between 30 and 120 arcmin (0.5° and 2°) are seen in similar robotic applications [36], [45]. Coupled to the high-torque motor, this transmission provides a continuous torque of 57.2 N·m and a peak torque of 182.6 N·m, demonstrating a larger scale application of an SPC-PGT transmission compared to the jumping robot in [45].

Finally, it is necessary to estimate the reflected inertia of the actuator with this choice of motor and transmission. We obtained this estimate by taking the inertias from the computer aided design (CAD) model of everything rigidly fixed to the motor's rotor, such as the motor shaft and sun gear, and multiplying it by the square of the gear ratio. We then added the inertias of all components that rotate with the actuator's output, such as the planet gears and carriers, to arrive at an estimated reflected

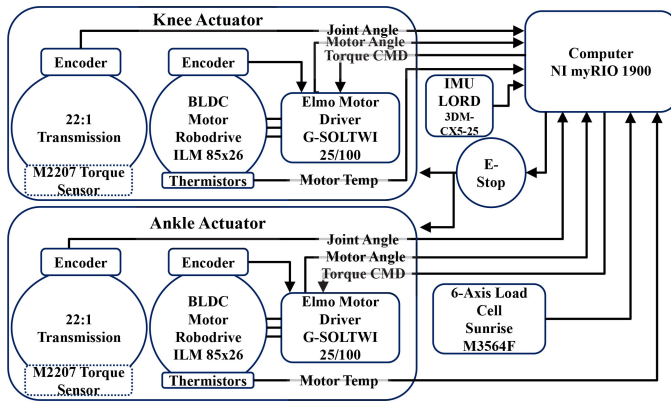


Fig. 4. Block diagram of electrical system: The system's computer receives feedback related to the user's gait and sends torque commands to the motor drivers. Torque sensors are indicated in dashed boxes to represent their presence during benchtop and AB testing but absence for amputee testing.

inertia of $I_j = 0.0625 \text{ kg}\cdot\text{m}^2$. This value is validated through benchtop experiments presented in Appendix A.

E. Sensors and Electrical System

Sensor feedback is critical for both the control and safety features of the device. The knee and ankle actuators have one optical quadrature encoder, E5 and EC35 (US Digital, Vancouver, WS, USA), with 4096 and 5000 cycles per revolution, respectively. Fixed to the motor shaft, the encoder sends motor position data to the motor driver and system controller. Once at the controller, these data are multiplied by the transmission reduction ratio for position and velocity feedback. The leg's design allows for a second encoder at the actuator output, which was used to quantify transmission backlash and then removed. For this reason, some renderings show two encoders per actuator. Additionally, both motors contain two Pt1000 thermistors embedded in the stator. These monitor the internal temperature of the stator to ensure that the motor is not damaged during use. A M3564F six-axis load cell, Sunrise Instruments, Nanning, China, is located below the ankle joint axis to detect ground contact and monitor ground reaction forces/moments. It is capable of reading 2500 N/200 N·m along the x and y axes and 5000 N/100 N·m along the z -axis. In addition to the load cell, a single axis M2207 torque sensor, Sunrise Instruments, Nanning, China, is located at the output of the knee and ankle actuators in the preliminary assembly used to validate the actuator capabilities, but not in the final assembly used for amputee testing.

These sensors interface with the system's microcontroller, a myRIO (National Instruments, Austin, TX, USA). The controllers presented in Sections III and IV are implemented in the National Instruments LabVIEW software environment and then imported onto the myRIO. Fig. 4 displays a systemic view of the described electrical system.

F. Knee Mechanical Structure

Although the physiological knee is a polycentric joint and many passive prostheses are modeled after this, powered prostheses are often modeled as a single-axis joint due to the minimal



Fig. 5. CAD design of the knee actuator. The exploded view on the left-hand side displays the components/subassemblies of the knee actuator, such as the upper/lower hinges, encoders, transmission, motor, and pylon. The image on the right-hand side presents the assembled knee actuator. The pyramid adapter on top connects to the user's socket, and the length-adjustable pylon on bottom connects to the ankle actuator module.

benefit gained from such an increase in design complexity [46], [47]. Therefore, the presented knee actuator shown in Fig. 5 is designed as a simple hinge, which includes an upper and lower hinge pieces. The upper hinge attaches to the socket on the user's residual limb via a pyramid adapter. The lower hinge is rigidly attached to the gearbox output (e.g., torque sensor), thus acting as the actuator output. Components of the actuator, such as the motor and transmission, are attached to the upper hinge, instead of the lower hinge, to minimize cable movement during gait. This design keeps the motor, transmission, and knee joint coaxial, which avoids the need for additional material/components to transfer motion from the motor axis to the knee joint axis.

This actuator is designed to allow simple changes to adjustable components so that the prosthesis may be configured for different use cases (i.e., modified range of motion and shank length). This is accomplished through the use of swappable hard stops and modular actuators separated by a pylon. Knee motion is constrained by bumpers that are 3-D printed using a compliant material, TangoPlus (Stratasys, Eden Prairie, MN, USA), to dampen the impact of the upper and lower hinges at maximum flexion and extension. Interchangeable bumpers of varying thickness allow the actuator to be configured with desired limits to knee flexion and extension. With no bumpers in place, the actuator's range of motion includes 112° flexion and -5° hyperextension.

Connected to the bottom of the lower hinge is an adjustable pylon system. This system consists of a universal PR pylon held by two tube clamps. Each tube clamp uses a single bolt to apply pressure around the circumference of the pylon, thus holding it in place. Due to this design, the distance between the two joints can be continuously adjusted for subjects with heights ranging from 1.52 to 1.98 m (5' to 6'6"), which can accommodate approximately 99.5% and 91.8% of all males and



Fig. 6. CAD design of the ankle actuator. The image on the left-hand side presents the assembled ankle actuator. The exploded view on the right-hand side displays the components/subassemblies of the ankle actuator, such as the motor, structure, four-bar linkage, transmission, electronics, and foot.

females, respectively [48]. The pylon can also be rotated by a prosthetist to properly align the abduction/adduction of the PR leg's ankle actuator.

G. Ankle Mechanical Structure

Similar to the knee actuator, the ankle is designed with a single axis of rotation. Although the concept and capabilities of the two actuators are the same (i.e., torque and velocities), the physical layout of the ankle actuator (see Fig. 6) is different from that of the knee. At the knee, the axis of rotation of the motor and the joint output are coaxial. At the ankle, the motor axis of rotation is moved proximal to the body for two main reasons: users apply greater hip torque and, therefore, expend more metabolic energy when wearing a mass that is more distal on the body [49], and overall actuator width would not allow the PR foot to wear a cosmetic foot shell or shoe. With the motor and the transmission moved proximal to the body, a parallelogram four-bar linkage mechanism was implemented to translate the torque from the output of the gearbox distal to the location of the anatomical ankle joint. Other powered PR ankles have utilized linkage mechanisms to alter joint torque or align impact loads [50], [51]. The ankle joint is mechanically constrained by hard stops located at approximately $\pm 45^\circ$. This provides ample rotation for a wide range of tasks while preventing excessive ankle flexion. The six-axis load cell is mounted directly below the ankle joint. An off-the-shelf Ottobock LoRider PR foot is attached to the bottom of the six-axis load cell. Finally, a cosmetic foot shell is installed onto the PR foot, allowing the user to wear most styles of shoes.

III. CONTROL METHOD

In this section, we present our approach for the control of the powered prosthesis. We show how the specific attributes of the designed actuator can be leveraged to facilitate the design of a dynamic walking controller.

A. Joint-Level Control

Due to its inherent simplicity and robustness, a proportional-derivative (PD) controller is the most common choice for controlling the joint position of robotic systems through the motor torque

$$\tau_m = \frac{1}{n} [K_p(\theta_d - \theta) + K_d(\dot{\theta}_d - \dot{\theta})] \quad (1)$$

where n is the transmission ratio, K_p and K_d are positive PD gains, and θ_d and θ are the desired and actual motor positions, respectively. Since the PD gains determine the pole's frequencies of the closed-loop system, these gains are set as high as possible to minimize tracking error and phase lag. In applications, such as PR legs, controllers that rely on a kinematic phase variable generally utilize this approach [14], [52], [53].

An alternative approach that is commonly used in control of powered prostheses is impedance control [54]. Generally, in robotics systems, the most common way to produce accurate joint impedance control is by using joint torque feedback to produce the desired behavior. Note that for a fixed transmission ratio n , the general relationship between motor torque τ_m and joint torque τ_j can be written as

$$\tau_j = n\tau_m + n^2 I_m \ddot{\theta} + n^2 b_m \dot{\theta} + f(\theta, \dot{\theta}, t) \quad (2)$$

where I_m and b_m are motor inertia and damping, respectively, θ is the joint angle, t is time, and f contains nonlinear and time-dependent losses, such as Coulomb friction, stiction, and hysteresis. Note that $\tau_m = k_t i_m$, where k_t is the motor's torque constant and i_m is its current, commanded from the motor driver. Torque feedback is typically necessary to decrease the effect of unmodeled dynamics (f) and common uncertainties of inertia and damping parameters in (2). However, an actuator designed with minimal unmodeled dynamics can be utilized to reliably simulate any desired dynamics (an arbitrary impedance, for instance) without requiring torque feedback. This is especially important in a control problem, such as walking, where unexpected interactions with the environment (impacts) are always likely to occur.

The high noise and limited speed of closed-loop force control during walking strongly motivates low-impedance actuation to achieve more natural dynamics. With an ideal actuator, a PD controller can be considered an open-loop impedance controller, with proportional and derivative gains acting as stiffness and damping, respectively [54]. Based on this, we expect that changing the stiffness and damping coefficients in (1) will enable a wide range of dynamic behaviors through highly variable joint impedances. Furthermore, the controller effectively can work as a position control scheme by increasing the gains, without any other change in the control structure.

As shown in [55], the discrete-time implementation of a controller in the form of (1) can lead to instability when the system interacts with a passive environment (in particular, a human). This depends on the human's emulated stiffness, actuator inertia and damping, and sampling frequency. Furthermore, it limits the range of the impedance coefficients (PD gains) that the controller can emulate. Based on this, we will later select the controller gains considering the actuator parameters and

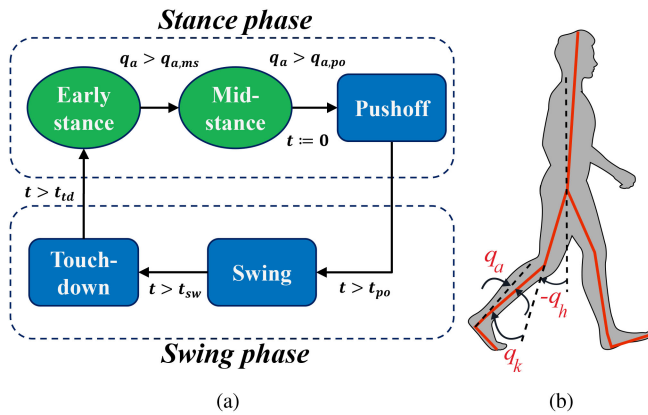


Fig. 7. (a) FSM for walking control. Blue rectangles and green ellipses indicate time-based (position control) and impedance-based states, respectively. (b) Definition of the joint angles.

the humans' applicable range of stiffness. See Appendix B for additional information regarding the stability of the selected values.

B. Walking Control

As discussed, the low-inertia design of the actuators facilitates smooth and easy switching between position and impedance control paradigms. Here, we show how this characteristic can be leveraged in a walking controller.

Sup *et al.* [18] designed a walking controller for their powered knee-ankle prosthesis based on a finite-state machine (FSM). For each state of the FSM, they used an impedance controller of the form

$$\tau_m = K_p(\theta_d - \theta) - K_d\dot{\theta} + K_2(\theta_d - \theta)^3 \quad (3)$$

where K_p , K_d , and K_2 are tunable constant values for each state. The form of the impedance controller (3) was chosen to fit human joint torque profiles. However, due to high impedance of the actuators, the final values of the tuned parameters were quite different from biological values. This implies that the total joint impedance is different from the commanded impedance due to the nonnegligible actuator impedance. The small correlation between the tuned and reference values of these parameters often requires lengthy sessions of tuning for each set of parameters to achieve the desired performance, since they are not known beforehand and change from one subject to another [35].

The controller we use in this work is similar to the one presented in [16]. Fig. 7 depicts the FSM corresponding to our controller. As in [16], impedance controllers have been used for control of early and mid-stance. This was motivated by the fact that impedance control provides reliable and smooth interaction with the environment (i.e., the ground). Since there is no interaction with the environment during swing phase, a time-based position tracking controller was designed based on AB reference trajectories [39]. In contrast with Sup *et al.* [18] wherein θ_d is constant for each subphase, we followed Lawson *et al.* [16] by tracking a time-based trajectory, which provides a stronger pushoff and a smoother transition to swing phase. Based on this,

time t is set to zero when the transition to pushoff takes place. The durations of pushoff, swing, and touchdown subphases are determined by the preset speed-dependent parameters t_{po} , t_{sw} , and t_{td} , respectively. At the start of each subphase, the change of parameters (K_p and K_d , and also θ_d for impedance-based subphases) is performed through the use of a third-order spline to avoid any discontinuity in the commanded torque.

The purpose of the touchdown subphase is to change the PD parameters for smooth transition to the impedance control of the early stance subphase. The idea is that as the knee extends, the controller “expects” the ground contact rather than sensing and then reacting to it. Thereby, the reaction to impact becomes a part of the natural (open-loop) dynamics of the system. This type of natural response is also observed in biological locomotion [56] and used in legged robot applications [57]–[59]. Based on this, gains are gradually changed throughout the touchdown subphase to match those of early stance. This smooth transition paradigm can be considered as an extension of the methods proposed in [60] and [61], in which transition to stance is detected without contact sensing. The main difference in these works is that the gains are held constant for each phase.

The default stiffness values (equivalent to K_p as discussed) for the impedance control subphases were picked from the quasi-stiffness of AB subjects, as estimated in [62], [63]. A small damping coefficient (K_d) was added to obtain a smoother operation. The details of the walking experiments and the selected gains are presented in the next section.

IV. EXPERIMENTS AND RESULTS

To validate and characterize the leg, benchtop and walking experiments were conducted. Benchtop experimentation aimed to verify specific characteristics of the actuators, whereas the walking experiments aimed to verify the leg's ability to perform under its designed loading conditions. A supplemental video of the experiments described in this section is available for download.

A. Benchtop Experiments

This section presents several benchtop experiments that demonstrate the position and impedance control capabilities, backdrivability, and bandwidth of the prosthesis' actuators.

1) *Backdrive Torque*: These tests aim to quantify the backdrive torque of the actuators, i.e., the torque required at the output of an actuator to rotate the motor through its transmission. For the first experiment, the ankle actuator was rigidly fixed to the benchtop setup with motion still being allowed at the ankle joint. A force was then applied with one finger to the toe of the foot [see Fig. 8(a)]. The applied force gradually increased until the joint moved. A total of nine trials of this experiment were conducted, three each with the ankle initially positioned at -20° , 0° , and 20° . For the case of 0° and 20° , a downward force was applied to result in plantar flexion. For the case of -20° , an upward force was applied to result in dorsiflexion.

Throughout this experiment, torque data were collected from the six-axis load cell. Torque maxima for each trial was extracted from the collected data and averaged for each initial starting

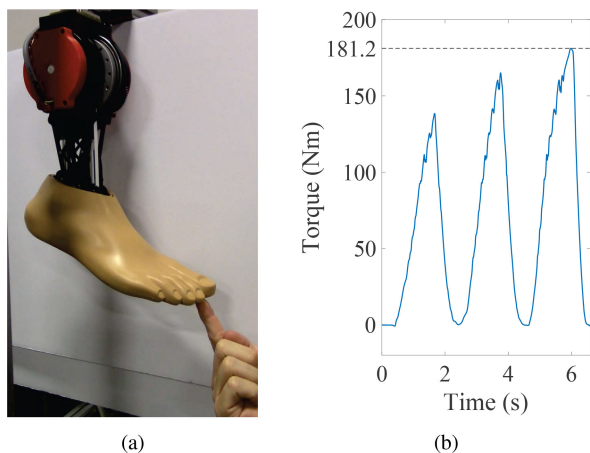


Fig. 8. Benchtop torque tests. (a) Experimental setup for backdrive torque test. (b) Measured torque during peak torque tests.

position. These maxima occurred directly before the applied torque overcame the backdrive torque within the system. The magnitudes of the mean peak torque values were 3.41, 3.23, and 3.22 N·m for the initial ankle positions of -20° , 0° , and 20° , respectively.

In another experiment, the knee actuator was fixed to the benchtop and its output disconnected. Starting at 0 N·m and with intervals of 0.1 N·m, the commanded torque was slowly increased until the joint started to move, which occurred at ~ 1 N·m. This consists of Coulomb friction and the uncompensated portion of cogging torque (depending on the cogging compensation methods used in the driver). Additionally, the Coulomb friction of the knee actuator, without the motor stator (in order to eliminate the cogging torque), was measured with a torque wrench to be ~ 0.2 N·m. These results suggest that the remaining backdrive torque can be attributed to the cogging torque of the motor. Therefore, we can conclude from these experiments that both actuators were able to be backdriven with low amounts of torque.

2) *Peak Torque*: To further verify the actuator capabilities, a simple test was conducted to quantify its peak torque. For this test, the knee and foot were separated from the ankle actuator. The ankle actuator was then fixed to the benchtop through the six-axis load cell, which measures the output of the ankle actuator. During this experiment, the position controller of the ankle actuator, presented in Section III-A, was set to regulate a fixed angle (zero). An oscillatory load was dynamically applied by hand to the shank. Note that this was intended to mimic how the prosthesis will interact with the ground during impedance-based states of the walking controller (see Section III-B). The pylon that typically connects the two actuators was replaced with an extended pylon to increase the lever arm and achieve larger torques. Force was applied by hand to the pylon for three consecutive cycles, with an increased magnitude for each cycle [see Fig. 8(b)]. The last force applied resulted in a peak measured torque of 181.2 N·m, which is ~ 1 N·m less than the peak rated torque of the actuator.

3) *Free Swing*: A free-swinging knee has the benefit of simplifying control effort during swing phase, therefore leading to

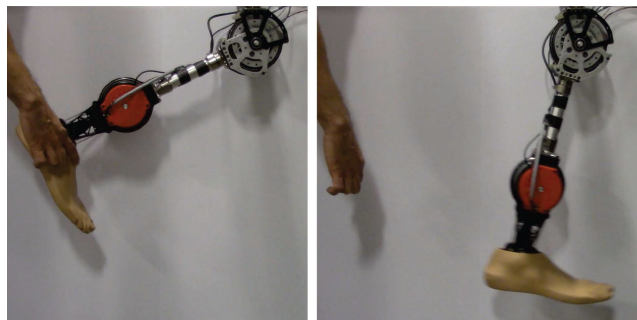


Fig. 9. Experimental setup for free swing test. The photo on the left-hand side shows the unpowered leg when the knee was held in flexion. The photo on the right-hand side shows the shank of the leg in motion after being released.

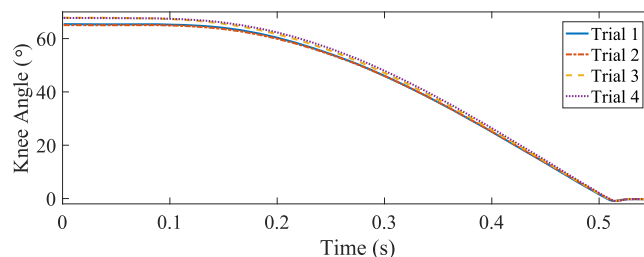


Fig. 10. Recorded position of the knee as it returns to zero following release from an initial offset.

more natural, energy-efficient operation. Toward this end, we performed a simple experiment to show that the knee could be backdriven by the weight of the shank and foot alone, thus simulating the swing phase of gait. With the motors unpowered, four trials were performed in which the top of the knee was fixed to the benchtop setup, flexed between 65° and 70° , and then released without a push. This experimental setup can be seen in Fig. 9. Fig. 10 shows the knee position for each of the four trials from the point of release until it reached the mechanical hard stop. With knee flexion peaking at approximately 70° for level walking, it can be seen in Fig. 10 that the knee exhibits free swing capabilities, since the knee repeatedly returns to zero after being released from heights common during walking.

4) *Closed-Loop Position Bandwidth*: Real-world physical systems generally act as low-pass filters, attenuating high-frequency inputs. In the case of actuators, especially electric ones, the cutoff frequency of the system becomes an important factor in characterizing the speed by which the output can be actively controlled through changing the input signal. Since closed-loop position controllers are implemented in some powered prostheses [14], [64], [65], closed-loop position control bandwidth tests were conducted to characterize the maximum frequency that the presented low-impedance actuators can achieve.

With the knee actuator fixed to the benchtop, the experiment began at a very low frequency, which was incrementally increased to higher frequencies until the test had to be halted due to excessive shaking and vibrations. The experiment was conducted with an input sine wave with three separate amplitudes: 5° , 10° , and 15° . The results, as shown in Fig. 11, indicate

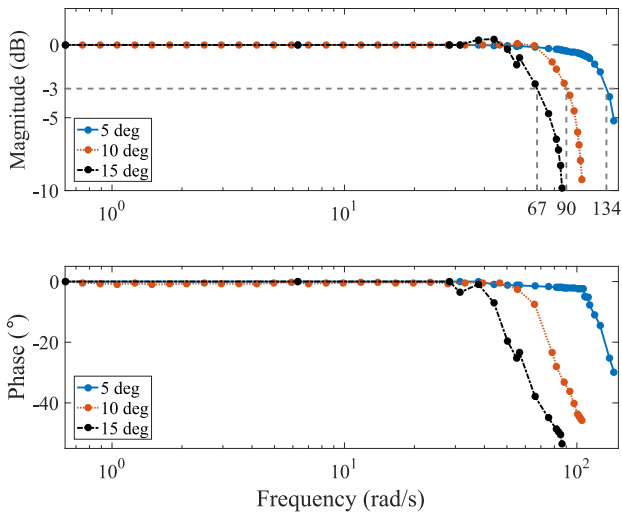


Fig. 11. Bode plots for closed-loop position bandwidth tests. Inputs with amplitudes of 5°, 10°, and 15° produce cutoff frequencies of approximately 134, 90.1, and 67.4 rad/s, or 21.3, 14.3, and 10.7 Hz, respectively.

respective cutoff frequencies of 134, 90.1, and 67.4 rad/s. Noting that a frequency analysis of human gait shows that the highest frequency content of walking is in the range of ~ 6 – 22 rad/s [39], [66], the actuator is expected to be completely capable of tracking the humanlike joint trajectories.

5) *Closed-Loop Position Control*: To examine the actuators' position-tracking capabilities, a PD controller with a gravity compensation term was implemented for each actuator. For this experiment, both joints were assembled together and the complete leg was mounted onto the benchtop setup, as shown in Fig. 9. The normative joint trajectories from Winter [39] were tracked at frequencies of 0.5 (slow walking), 1.0 (fast walking), and 1.3 Hz (running) [66].

Fig. 12 displays tracking performance per joint for the increasing frequencies. For all three frequencies, the ankle actuator was able to track the position with little error (max 0.27°, 0.45°, and 0.55° for 0.5, 1, and 1.3 Hz, respectively). Although the knee tracking errors were relatively small for 0.5 and 1 Hz (max 1.04° and 6.42°, respectively), at 1.3 Hz, the difference between desired and actual trajectories starts to become visible (max 13.17°). This error was mainly due to phase lag between desired and measured trajectories. Neglecting this phase lag reduces the maximum knee tracking error to 2.05° and 4.56° for 1 and 1.3 Hz, respectively. The higher error in the knee angle was due to both larger mass and inertia acting against the knee actuator, as well as the larger range of motion and higher acceleration compared to the ankle. Note that joint torque was limited to ± 120 N·m for safety during these benchtop tests. This limitation will be relaxed for walking experiments, which will also have an aiding hip moment to swing the knee.

6) *Open-Loop Impedance Control*: In the previous sets of experiments, we showed that the design of the actuator and its high bandwidth make it capable of supporting walking control paradigms based on precise joint position tracking. Here, we show that the actuator design also works well for compliant walking control paradigms (as discussed in Section III). This

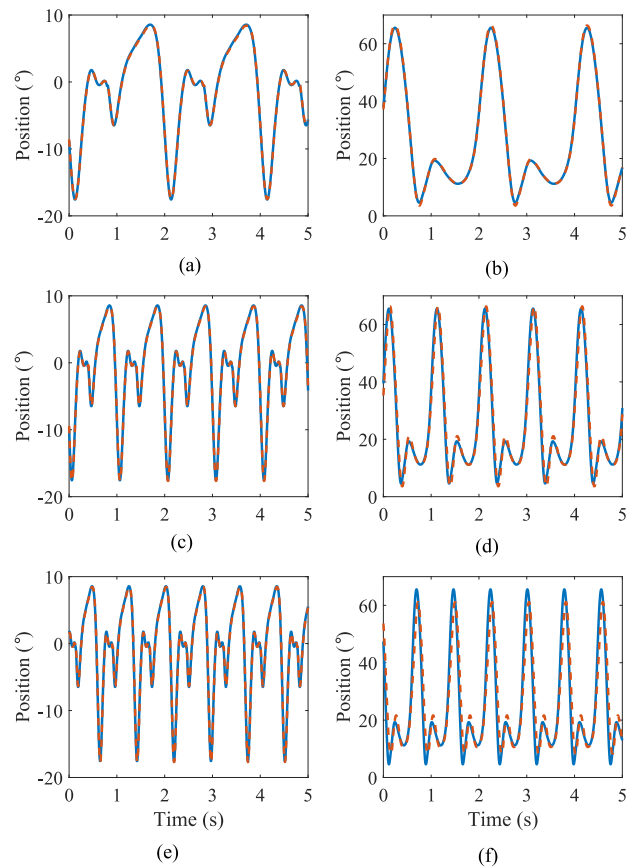


Fig. 12. Position tracking of normative gait trajectories at various frequencies. Solid blue and dotted red lines denote the desired and measured position, respectively. (a), (c), and (e) Ankle tracking at 0.5, 1, and 1.3 Hz, respectively. (b), (d), and (f) Knee tracking at 0.5, 1, and 1.3 Hz, respectively.

specifically becomes important when one considers the most difficult portions of human trajectories to be mimicked by position control, namely the quick flexion and extension of the knee immediately after impact [see Fig. 12(f)]. In humans, this happens due to natural compliance of the knee joint, rather than precisely following a prescribed position trajectory [46], [62]. This motivates us to test the ability of the designed actuator to demonstrate specific impedance behaviors.

As discussed in Section III-A, we simply set the position control PD gains, K_p and K_d , equal to the desired spring and damper coefficients with units of newton meter per radian and newton meter second per radian, respectively. During these experiments, the position control was set to regulate a fixed angle (zero) as a person tried to move the ankle joint by hand, as shown in Fig. 8(a). The six-axis load cell was used at the joint to measure the torque applied by the person (which is the same as joint torque), and compare it to the commanded torque.¹ In an ideal case, these two torques will be equal, i.e., $\tau_j = n\tau_m$.

Fig. 13 depicts the resulting ankle torques of four different experimental cases. The first case [see Fig. 13(a)] shows a pure damping test ($K_p = 0$ and $K_d = 29$). The commanded torque

¹Note that the load cell was merely used for measurements and not for any kind of feedback control since the control paradigm does not require it. However, future controllers may require its feedback.

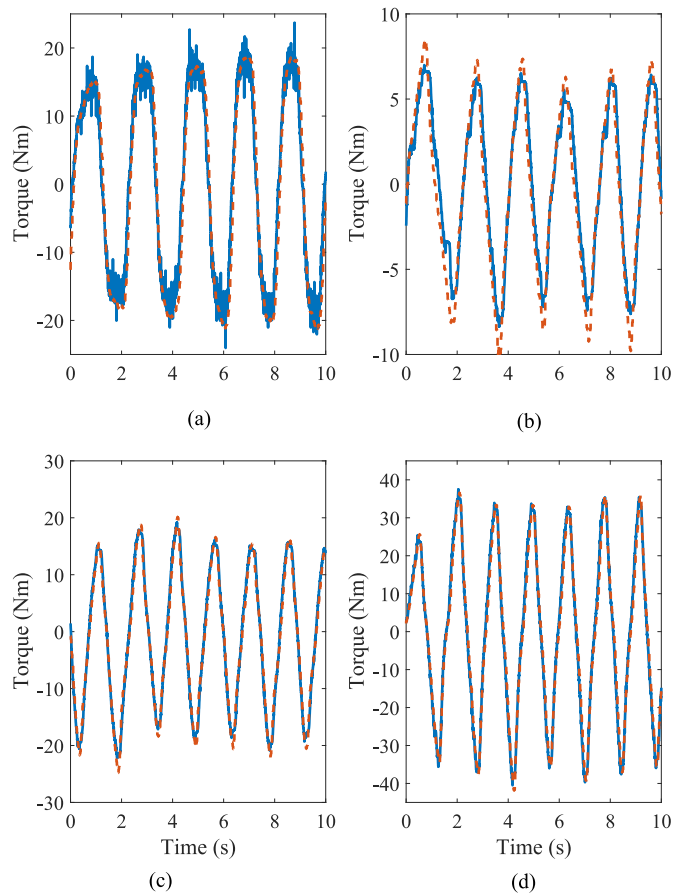


Fig. 13. Open-loop impedance of the ankle joint with various K_p and K_d gains. Solid blue and dotted red lines correspond to commanded and measured torque, respectively. PD gains used are: (a) $K_p = 0$ and $K_d = 29$, (b) $K_p = 46$ and $K_d = 3$, (c) $K_p = 46$ and $K_d = 3$, and (d) $K_p = 172$ and $K_d = 9$.

has noise when the torque changes directions because this case only uses damping with joint velocity feedback, which has noise from taking the time derivative of the encoder reading. Cases two and three [see Fig. 13(b) and (c)] show low stiffness, reduced damping tests ($K_p = 46$ and $K_d = 3$) at small and large torques, respectively. Finally, case four in Fig. 13(d) depicts a combined stiffness-damping control ($K_p = 172$ and $K_d = 9$). The figures show a strong agreement between measured joint torque and commanded motor torque in cases (a), (c), and (d), demonstrating that the effect of unmodeled dynamics is negligible for torques over ~ 10 N·m. Note that joint torques are much larger than 10 N·m during the stance phase of walking [39], making the actuator suitable for any type of compliant control during stance. The unmodeled dynamics only become apparent during the low torque tests, where a noticeable difference exists for amplitudes less than ~ 5 N·m [see Fig. 13(b)]. Interestingly, the difference between joint and commanded torque is around the previously observed value for the backdrive torque (~ 3 N·m).

Using the measured joint torque from the load cell and the measured angle and velocity from the encoder, we identified K_p and K_d values from (1) as: $K_p = 0$ and $K_d = 23$, $K_p = 46$ and $K_d = 2$, $K_p = 46$ and $K_d = 2$, and $K_p = 172$ and $K_d = 7$. These closely resemble the prescribed values used for each

TABLE III
SUBJECT SPECIFIC INFORMATION

Subject	Height (m)	Age (yrs)	Weight (kg)	Passive Knee	Passive Ankle
AB	1.760	39	73	N/A	N/A
TF	1.798	62	104	Rheo Knee XC	Pro-Flex XC Torsion



Fig. 14. Experimental setup for AB walking experiments. The image on the left-hand side shows the subject, safety harness, treadmill, and sound-level meter. The image on the right-hand side shows how the PR leg was connected to the bypass adapter, and how it was attached to the subject's leg.

individual test, especially K_p values. The least squares method was used to quantitatively evaluate the closeness of commanded torques, determined using the prescribed and identified gains in (1). For all trials, the coefficient of determination between the prescribed-commanded torque and the identified-commanded torque is 0.999, or $R^2 \cong 1$. The strong agreement between these values further proves that the effects of the system's unmodeled dynamics are negligible.

B. Walking Experiment Methods

Walking experiments were conducted with one AB subject and one TF (above-knee) amputee subject. AB experiments aimed to assess and validate the capabilities of the hardware, whereas TF experiments aimed to assess clinical performance of the leg under the loading conditions for which it was designed. The AB experiment was conducted first using the original leg assembly with the joint torque sensors. After validating the leg's torque/power capabilities in the AB experiment, the torque sensors were removed in the revised assembly described in Section II-B for the TF experiment. Note that the AB subject was an expert user of powered prostheses, having substantial experience walking on such devices. In contrast, the TF subject had never walked with a powered prosthesis prior to these experiments. Subject specific information and measurements are presented in Table III.

Using the walking controller in Section III-B, both subjects walked on the leg at different speeds on a treadmill (see Figs. 14

TABLE IV
SPEED-INDEPENDENT CONTROL PARAMETERS

	K_p (ankle)	K_d (ankle)	θ_d (ankle)	K_p (knee)	K_d (knee)	θ_d (knee)	$q_{a,ms}$
Early stance	246	11	0	284	11	0.09	-
Mid-stance	992	17	0.07	284	11	0.09	0.07
Pushoff	-	17	time-based	458	11	time-based	-
Swing	688	17	time-based	573	23	time-based	-

Note: Parameters K_p and K_d are in newton meter per radian and newton meter second per radian, respectively, and $q_{a,ms}$ and θ_d are in radians. Stance K_p are according to biological stiffness estimates from [62] and [63].

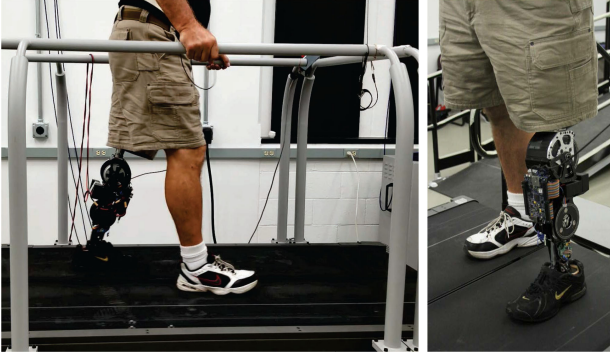


Fig. 15. Experimental setup for amputee walking experiments. Both images show the amputee subject wearing the prosthesis on the instrumented treadmill. Note that although the batteries were mounted to the leg during these experiments, the leg was powered by identical off-board batteries to allow for the off-board measurement of current and voltage.

and 15). All experimental procedures were approved by The University of Texas at Dallas Institutional Review Board, and signed consent was obtained from each subject prior to testing. The AB subject wore the PR leg through a custom bypass adapter and a shoe lift on the non-PR leg to equalize their leg length to that of the PR leg. A practicing, certified, and licensed prosthetist was present during the TF subject's experiment. This prosthetist fit and aligned the PR leg directly on the TF subject's personal socket. While walking on the treadmill, both subjects wore a safety harness around their torso to prevent injury in the case of tripping or falling. An emergency stop button, which would disable the motors when pushed, was given to the subjects if they felt the need to stop at any time.

Each subject was asked to walk on the treadmill for approximately 60 s at a range of walking speeds (0.9, 1.1, 1.3, and 1.6 m/s) while wearing the powered PR leg. In order to follow the speed-independent results of the work in [62] and [63], K_p and K_d values corresponding to impedance control states were held constant across speeds. The swing-phase PD gains were also held constant because of their negligible effect across different walking speeds. For the AB subject, only the pushoff ankle gains (K_p) were tuned until the subject felt a comfortable propulsion force. Moreover, only pushoff timing variables and one K_p value were tuned to be different for the TF subject relative to the AB subject. All other gains were kept consistent across subjects to display the potential for reduced tuning time. Tables IV and V summarize the parameters used for these trials.

TABLE V
SPEED-DEPENDENT CONTROL PARAMETERS

Subject	Speed	K_p (ankle, pushoff)	$q_{a,po}$	t_{po}	t_{sw}	t_{td}
AB	0.9 m/s	344	0.14	0.55	0.86	0.95
AB	1.1 m/s	401	0.13	0.47	0.74	0.82
AB	1.3 m/s	458	0.12	0.40	0.63	0.70
AB	1.6 m/s	458	0.11	0.30	0.54	0.60
TF	0.9 m/s	286	0.10	0.35	0.58	0.65
TF	1.1 m/s	401	0.10	0.35	0.54	0.60
TF	1.3 m/s	458	0.10	0.35	0.54	0.60
TF	1.6 m/s	458	0.09	0.25	0.44	0.50

Note: Parameters K_p and $q_{a,ms}$ are in newton meter per radian and radian, respectively, and times are in seconds.

The acclimation/tuning period before recording data with the TF subject lasted less than 30 min.

Throughout the trials, gait kinematics and kinetics were collected for validation of the PR leg. Disregarding gait acceleration and deceleration at the beginning and end of the walking trial, 30 s of continuous, steady-state walking was captured for each speed. The data were divided and normalized by stride, which in turn allowed the calculation of gait statistics, such as means and standard deviations. To further study the actuator design during gait, two other measurements were recorded: power drawn from the battery and acoustic sound levels. To evaluate the electrical power consumption and regenerative capabilities of the leg, a current probe, TCPA300 (Textronix, Beaverton, OR, USA), was used to measure real-time current flowing to and from the entire leg. Current measurements, along with the battery's voltage, were recorded by an offboard oscilloscope, DPO 2024B (Textronix), and saved to an offboard computer. Finally, to investigate the acoustic sound level of the powered PR leg, a PCE-322 A sound-level meter (PCE Instruments, Jupiter, FL, USA) recorded the magnitude of sound coming from the leg during the walking trials. The sound meter was placed at the height of the user's ear, approximately 1.5 m away, to measure the magnitude of the sound heard from their perspective. Note, that sound-level measurements were only taken during AB trials.

C. AB Walking Results to Validate Leg Capabilities

This section presents the results from the AB experiment to validate the performance capabilities of the prosthesis with the

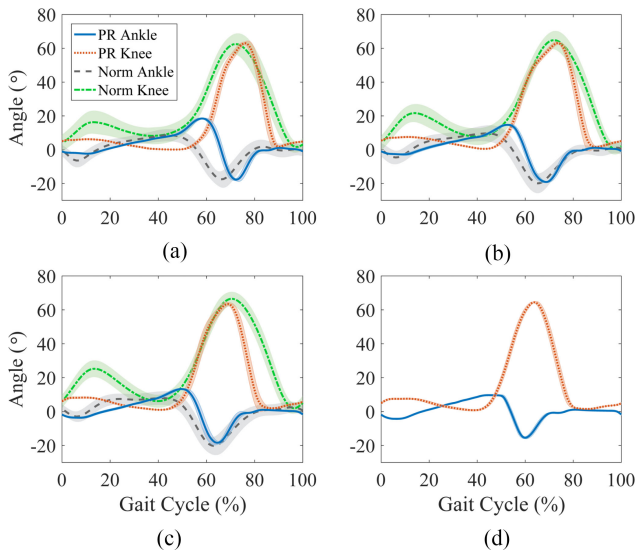


Fig. 16. PR knee and ankle joint position during AB walking with the prosthesis. Solid blue and dotted red lines correspond to the average ankle and knee joint angles, respectively, for speeds: (a) 0.9 m/s, (b) 1.1 m/s, (c) 1.3 m/s, and (d) 1.6 m/s. Standard deviations (± 1) are indicated by shaded regions around the mean. Normative (Norm) knee and ankle trajectories [39] (not available for 1.6 m/s) are shown as a reference in green dash-dotted and gray dashed lines, respectively.

torque sensors, specifically the kinematic and kinetic outputs, electrical and mechanical power output, and acoustic noise.

1) *Kinematic and Kinetic Analysis*: Fig. 16 shows the collected knee and ankle joint angles for different walking speeds and compares them to healthy (normative) gait kinematics [39]. Note that the healthy dataset in [39] does not include high-speed gaits for inclusion in Fig. 16(d). The gait cycle begins and ends at ground impact of the prosthesis, with the transition from stance to swing occurring around 60% of the gait cycle.

Figs. 17 and 18 depict the commanded versus measured torques of the knee and ankle joints, respectively, during walking experiments. As expected from the results of the benchtop tests, the commanded and measured torques closely match, confirming the hypothesis regarding low actuator impedance and unmodeled dynamics. One notable difference is at peak negative torques in Fig. 18. At this point in gait, the excessively large joint acceleration makes the motor's inertia contribute more to the unmodeled dynamics of the actuator. However, since the joint's acceleration is larger than what is seen in healthy gait [39], we expect this discrepancy to be mitigated in future control schemes that better limit the joint's acceleration to normative values.

These biomechanical results demonstrate that the PR leg can indeed perform as intended across walking speeds, and justify removing the torque sensors in the revised leg assembly used for amputee testing in Section IV-D.

2) *Power Capabilities*: This section examines the ability of the leg to output sufficient power during walking. Fig. 19 displays the leg's electrical and mechanical power over the average stride at each speed condition. The combination of the leg's current i and voltage V allows for the calculation of the PR leg's total or consumed electrical power at each instant, $P_E = i \cdot V$.

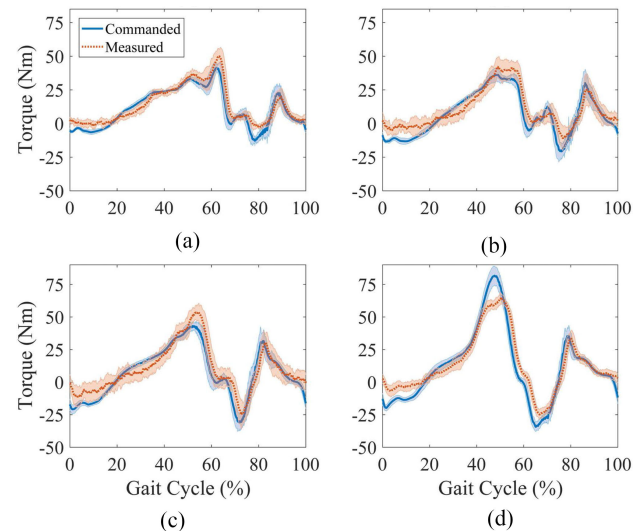


Fig. 17. Average knee commanded and measured torque during AB gait. Solid blue and dotted red lines correspond to the commanded and measured torque, respectively, for speeds: (a) 0.9 m/s, (b) 1.1 m/s, (c) 1.3 m/s, and (d) 1.6 m/s. Standard deviations (± 1) are indicated by shaded regions around the mean.

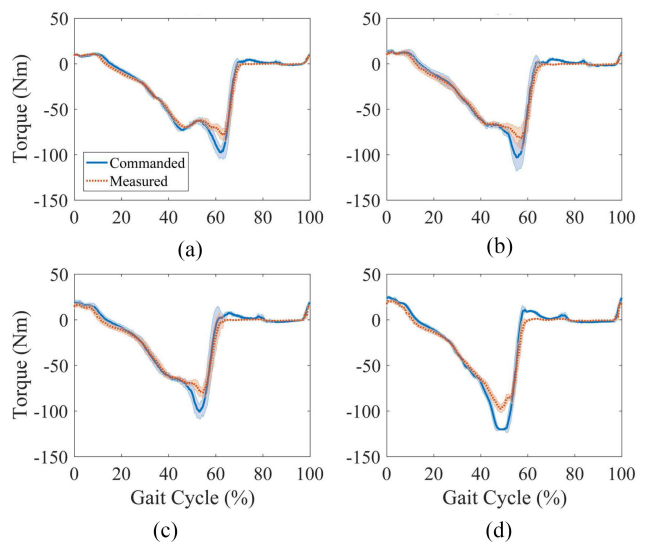


Fig. 18. Average ankle commanded and measured torque during AB gait. Solid blue and dotted red lines correspond to the commanded and measured torque, respectively, for speeds: (a) 0.9 m/s, (b) 1.1 m/s, (c) 1.3 m/s, and (d) 1.6 m/s. Standard deviations (± 1) are indicated by shaded regions around the mean.

This power is compared against the leg's total output mechanical power of both joints, $P_M = \tau_K \cdot \omega_K + \tau_A \cdot \omega_A$, where τ is measured joint torque, and ω is measured joint velocity; indices K and A indicate values relating to the knee and ankle joints, respectively. Fig. 19 also displays the individual knee mechanical power ($P_K = \tau_K \cdot \omega_K$) and ankle mechanical power ($P_A = \tau_A \cdot \omega_A$).

Peak mechanical powers for the knee were 236.7, 192.1, 298.7, and 389.4 W, and the ankle peak mechanical powers were 246.1, 275.4, 294.2, and 371.6 W for 0.9, 1.1, 1.3, and 1.6 m/s, respectively. Peak specific powers (normalized by the subjects

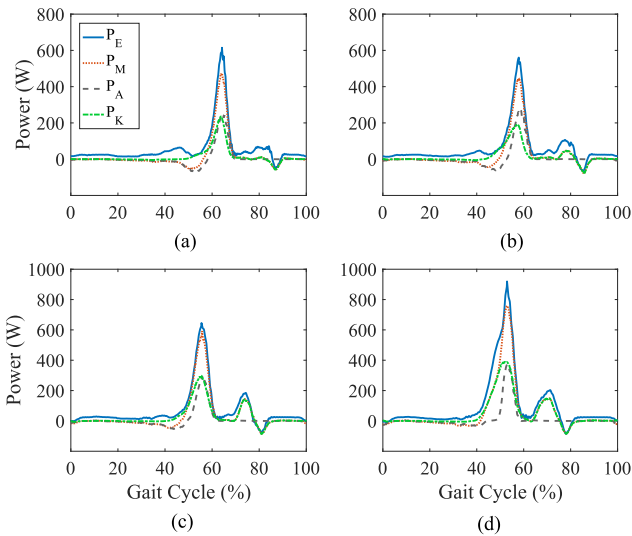


Fig. 19. Average power per gait cycle of the PR leg at different walking speeds for the AB subject at (a) 0.9 m/s, (b) 1.1 m/s, (c) 1.3 m/s, and (d) 1.6 m/s. Solid blue lines indicate power calculated from measured current and voltage to and from the batteries. Dotted red lines indicate power calculated from measured torque and velocity. Dashed gray and dash-dotted green lines indicate mechanical joint power from measured torque and velocity for the ankle and knee, respectively.

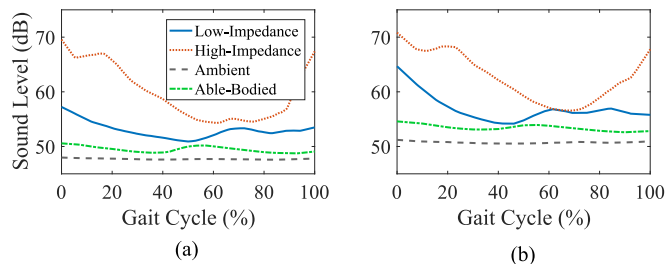


Fig. 20. Acoustic sound level during gait at (a) 0.9 m/s and (b) 1.3 m/s. Solid blue, dotted red, dashed gray, and dash-dotted green lines represent the presented PR leg with low-impedance actuators, a traditional powered PR leg with high-impedance actuators, an AB subject, and ambient sound levels, respectively, during treadmill walking. Ground contact of the PR leg starts at 0% of the gait cycle.

mass) were 3.24, 2.63, 4.09, and 5.33 W/kg for the knee, and 3.37, 3.77, 4.03, and 5.09 W/kg for the ankle across speeds.

3) *Acoustic Sound Level*: Fig. 20 compares the sound level of the presented PR leg to a previously published leg that utilizes high-impedance actuators [67]. Note that the y-axis scale (dBA) is not linear, but logarithmic. In this figure, the gait cycle begins and ends at ground impact, with the transition from stance to swing occurring at about 60% of the gait cycle. It is evident that the leg with low-impedance actuators is much closer to the sound level of AB walking than the leg with high-impedance actuators. As speed increases, the ambient, AB, and low-impedance leg's sound levels were generally shifted upward in the figure, which is related to the increased sound of the treadmill. In fact, the difference between AB and the low-impedance actuator's sound levels was fairly similar across speeds, not considering impact with the ground. Note that due to the low sampling rate of the sound-level meter (10 Hz), large changes in sound-level readings may look like instantaneous jumps in data, which explains why

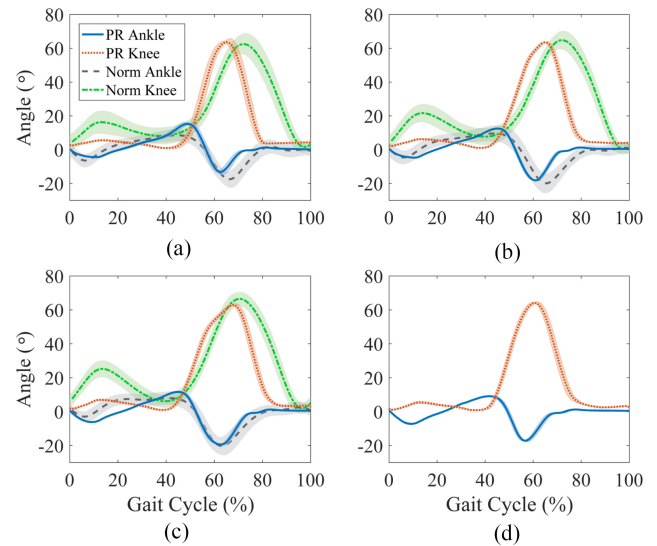


Fig. 21. PR knee and ankle joint position during amputee walking with the prosthesis. Solid blue and dotted red lines correspond to the average ankle and knee joint angles, respectively, for speeds: (a) 0.9 m/s, (b) 1.1 m/s, (c) 1.3 m/s, and (d) 1.6 m/s. Standard deviations (± 1) are indicated by shaded regions around the mean. Normative (Norm) knee and ankle trajectories [39] (not available for 1.6 m/s) are shown as a reference in green dash-dotted and gray dashed lines, respectively.

the values at 0% and 100% do not align for all cases. Interestingly, these instantaneous jumps between endpoints were not seen in the traditional actuation style. This likely due to the large velocities, and therefore increasing sound, of the PR actuators leading up to impact. Therefore, we can conclude that since the low-impedance actuators are much quieter than the high-impedance actuators, ground-impacts and ambient sound levels have a greater contribution to the sound level of walking with low impedance actuators.

It is evident that the low-impedance actuation is much quieter than the traditional actuation. Specifically, the presented leg is on average 7 and 6 dB quieter (including impacts) than that of the conventional powered leg at 0.9 and 1.3 m/s, respectively. If impacts were disregarded, we expect the difference would be much greater.

D. Amputee Walking Results to Assess Clinical Performance

This section presents the results from the amputee experiment to assess clinical performance of the prosthesis without the torque sensors. Specifically, we assess the normality of gait kinematics and the power consumption of the prosthesis during amputee walking conditions.

1) *Kinematic Analysis*: Fig. 21 shows the collected knee and ankle joint angles of the prosthesis during TF walking at different speeds, and compares them to healthy (normative) gait kinematics [39]. Although the subject typically preferred that pushoff began earlier in the gait cycle than healthy averages, their joint kinematics resemble that of healthy joints in terms of magnitudes and general trends. Specifically, as speeds increase, pushoff shifts earlier in the gait cycle. Furthermore, the early pushoff resulted in a decreased PR stance phase and, therefore,

TABLE VI
AVERAGE ENERGY (J) IN JOULES AND EFFICIENCY (η) OF THE LEG PER GAIT CYCLE DURING AMPUTEE WALKING

	J_{P_K}	J_{R_K}	J_{P_A}	J_{R_A}	J_{P_M}	J_{R_M}	J_{P_E}	J_{R_E}	η (%)
0.9 m/s	5.9	-10.4	9.5	-13.8	13.0	-21.8	27.4	-6.7	40.1
1.1 m/s	7.8	-15.0	7.7	-12.4	9.7	-21.6	21.8	-7.4	39.4
1.3 m/s	8.4	-18.7	7.4	-13.3	9.3	-25.5	21.4	-11.2	43.7
1.6 m/s	21.3	-14.4	17.8	-12.5	36.8	-24.6	57.6	-11.4	58.7

Note: Subscripts P and R indicate energy produced and regenerated, respectively. K and A indicate mechanical energy of the knee and ankle joint, respectively. M indicates the combined mechanical energy of both joints. E indicates electrical energy from the battery.

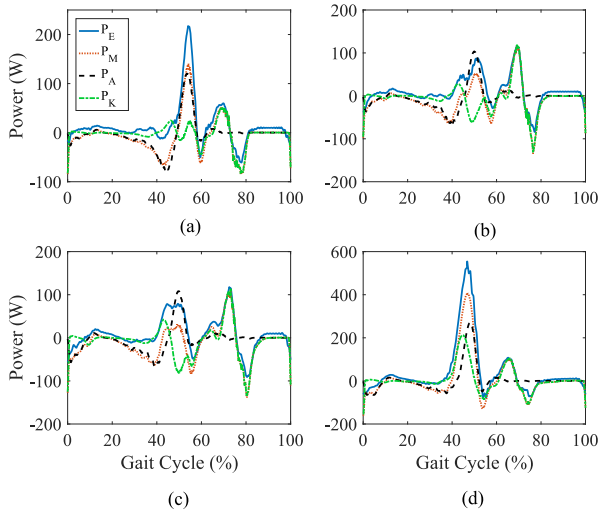


Fig. 22. Average power per gait cycle of the PR leg at different walking speeds for the amputee subject at (a) 0.9 m/s, (b) 1.1 m/s, (c) 1.3 m/s, and (d) 1.6 m/s. Solid blue lines indicate power calculated from measured current and voltage to and from the batteries. Dotted red lines indicate power calculated from measured torque and velocity. Dashed gray and dash-dotted green lines indicate mechanical joint power from measured torque and velocity for the ankle and knee, respectively.

a prolonged PR swing phase, which is common in amputee gait. This resulted in a longer period of knee extension before heel strike. However, this affect was diminished at faster speeds, where the kinematics became more normative.

2) *Power and Energy Analysis*: Fig. 22 presents the power of the prosthesis during walking with the TF subject, similar to the AB case in Section IV-C.2. Because the torque sensors were removed in the TF case, the power is based upon commanded torque τ and measured velocity ω , where we previously saw that commanded torque is an accurate representation of actual torque. By integrating these curves, electrical and mechanical energies were calculated and presented in Table VI. Positive values in this table indicate produced energy (integral of power greater than zero), whereas negative values indicate regenerated energy (integral of power less than zero). Specifically, J_{P_K} , J_{R_K} , J_{P_A} , and J_{R_A} indicate produced knee, regenerated knee, produced ankle, and regenerated ankle mechanical energies, respectively. Furthermore, J_{P_M} and J_{R_M} indicate the produced and regenerated mechanical energies of the combined joints (i.e., from P_M). Note that these two values do not directly equal the sum

of the produced or regenerated energies of the individual joints. Instead, they arise from the combined joint mechanical energies of the leg as a whole, which accounts for power sharing between the joints. The total efficiency of the prosthesis is defined as $\eta = (|J_{R_E}| + J_{P_M}) / (J_{P_E} + |J_{R_M}|)$, where J_{P_E} and J_{R_E} are the produced and regenerated electrical energies, respectively. The numerator accounts for the “output” energy flowing to the battery and environment, and the denominator accounts for the “input” energy flowing from the battery and environment. Note that as speed increases, efficiency also increases. One contributing factor to this was the constant 20 W consumed by the electronics and on-board computer, which has more influence on the efficiency relative to mechanical power during slow walking. Moreover, at slower walking speeds, the motors provide torques at lower velocities, where the electric motor is less efficient due to winding losses.

Similar to the AB case, the TF subject shows regions where rapid deceleration of joints cause power regeneration. This is most evident in Fig. 22, between approximately 75% and 80% of the gait cycle. We also see regions where power was being shared between the joints, such as Fig. 22(a)–(c) between approximately 35% and 45% of the gait cycle, where the ankle mechanical power was negative, whereas knee power was positive. Interestingly, this is also seen in Fig. 22(a) and (b) at approximately 50% of the gait cycle, which allowed for an ankle mechanical power that was larger than the electrical power to the entire leg. This was caused by the large regenerative power of the knee during the same instance, which reduced the power demand from the batteries.

Both energy sharing and regeneration aid in reducing the average energy consumed per gait cycle. Our new PR leg has an average specific power of 0.14, 0.11, 0.08, and 0.40 W/kg (normalized by the subject’s mass) for 0.9, 1.1, 1.3, and 1.6 m/s, respectively. With the selected batteries, the PR leg can currently operate for 2.82, 3.74, 4.92, and 0.99 h of continuous walking, or 7301, 10 514, 14 875, and 3263 PR steps at each respective speed. Note that the total step count for the user would double when considering the intact limb.

V. DISCUSSION

A. Advantages of Design

The main objective of this work was to achieve low-impedance actuation in a powered PR leg and to analyze its

TABLE VII
COMPARISON OF INERTIAS, TRANSMISSION RATIOS, AND JOINT TORQUE OF PR LEG ACTUATORS

	Motor	Motor Inertia 10^{-4} (kg·m ²)	Gear Ratio	Rotor Reflected Inertia at the Joint (kg·m²)	Continuous Joint Torque (N·m)	ρ (N·m/kg·m ²)
Low-Impedance Leg	Robodrive ILM 85x26	1.1500	22:1	0.0557	57.2	1027
UTD Leg 1 - Knee¹ [14]	Maxon EC-4 pole 30	0.0333	360:1	0.4316	34	80
UTD Leg 1 - Ankle¹ [14]	Maxon EC-4 pole 30	0.0333	720:1	1.7263	69	40
VU Leg Gen. 3 - Knee [16]	Maxon EC-4pole 30	0.0333	176:1	0.1032	17	165
VU Leg Gen. 3 - Ankle [16]	Maxon EC-60	1.1950	115:1	1.5804	46	29
Open-Source Leg - Knee [25]	T-Motor U8	1.3000	49.4:1	0.3172	47	148
Open-Source Leg - Ankle¹ [25]	T-Motor U8	1.3000	58.4:1	0.4434	55	125
Ampro [69]	Moog BN34	0.0510	80:1	0.3264	34	104
CMU Leg [70]	Robodrive ILM 85x13HS	0.6100	50:1	0.1525	71.5	469
Utah AVT Knee¹ [24]	Maxon EC-4pole 22	0.0089	25-375:1	0.0006-0.1252	1-20	1667-0.01
Utah Polycentric Ankle¹ [50]	Maxon EC-4pole 30	0.0333	120-800:1	0.0479-2.1312	11-76	229-36

Based on estimated average transmission ratios since actual ratios can vary based on joint kinematics.

performance. Initial benchtop tests concluded that with the motors OFF, the actuators have sufficiently low impedance, with a backdrive torque of $\sim 1-3$ N·m and free swing capability. Other tests demonstrated that even with low-impedance actuators, the prosthesis was still able to provide very large torque (>180 N·m), thus satisfying our torque design goals. Furthermore, by measuring the actuator's open-loop frequency response (see Appendix A), we found the actuator's inertia to be $I = 0.0696$ km·m², which is very close to the estimated inertia from the CAD model, $I = 0.0625$ km·m², and is less than the state-of-the-art leg in [16].

For context and comparison, Table VII presents the estimated reflected inertias of the actuators in several other powered prostheses. Note that in this table, values for reflected inertia only consider the motor rotor inertia and transmission ratio, omitting the inertias of the transmission components (hence, the presented actuator's inertia is reported as 0.0557). This was done for consistency when comparing across actuators, since we do not have access to the CAD models or system identification data for these prostheses. Moreover, when comparing actuators, it is also important to compare torque capabilities since an actuator's reflected inertia can easily be reduced at the cost of torque. Therefore, Table VII also presents the ratio of continuous (nominal) joint torque to joint reflected inertia ρ . Larger values of ρ indicate an actuator's ability to achieve large continuous torques with respect to its reflected inertia.

Note that the Utah AVT knee [24] is the only prosthesis that has a larger ρ than that of the presented prosthesis. This is achieved when its actively variable transmission minimizes its reduction ratio, therefore minimizing the reflected inertia of the actuator. However, to do this, the subject must stop and unload the prosthesis for a short period of time while the transmission adjusts, which does not allow for quick switching between low impedance and high torque. This is most important during the pushoff phase of gait when the leg requires large torques immediately followed by low impedance, which allows for knee free swing and rapid ankle dorsiflexion for toe clearance.

Similarly, the Utah Polycentric Ankle prosthesis [50] has a variable transmission with a minimum reflected inertia (0.0479) at approximately 20° of dorsiflexion, but it has a larger reflected inertia than the presented prosthesis throughout the majority of its range of motion. On the other hand, the presented prosthesis inherently has low impedance, and can switch to high stiffness/torque very quickly, which makes it desirable for pushoff and very suitable for other highly dynamic or extreme tasks. Although it is unrealistic to reduce the joint reflected inertia to that of a human joint, which is considered negligible [39], we were able to achieve a compromise between low reflected inertia and high torque to increase ρ compared to other prostheses. In addition to having the largest constant ρ , and to the best of our knowledge, the presented actuators can produce the largest torque of any self-contained powered prosthesis throughout the literature. The tradeoff in terms of weight is discussed in Section V-B.

Open-loop impedance control tests demonstrated that the effects of unmodeled actuator dynamics are negligible for torques over ~ 10 N·m. The strong agreement of commanded and measured joint torques during AB walking confirmed this hypothesis during gait. Moreover, the compliant nature of the actuators, coupled with the implementation of human joint impedances, allowed the joints to naturally favor biological reference trajectories during the stance phase of gait. These trends are evident in both the AB and TF walking experiments, indicating the potential for simplifying the tuning process compared to traditional actuation schemes. Although further optimization and tuning would be necessary to more closely match normative trajectories, the presented walking experiments demonstrate the possible reduction in tuning time when human joint impedances are directly implemented.

In addition to accurate impedance control, the actuators maintain the ability to accurately control position. This was first demonstrated in benchtop experiments, where the leg successfully tracked positions for frequencies up to 1.3 Hz with

negligible error. As the frequency of the trajectory increases, the first visible discrepancy between desired and actual trajectories in Fig. 12 appears at knee flexion and extension immediately after the touchdown phase. In this region of gait, active position tracking is not strictly required because the function of the knee is to absorb energy, which was achieved through impedance control in walking experiments.

Across all speeds in the AB walking experiments, the PR leg's knee and ankle angles (PR knee and PR ankle) were similar to that of the normative knee and ankle reference trajectories (norm knee and norm ankle) in Fig. 16. Slight discrepancies were seen at some speeds because the controller utilizes reference trajectories for normal walking speed (1.1 m/s), which explains why joint angles were qualitatively similar to the normative trajectories in Fig. 16(b). Furthermore, AB walking experiments demonstrated increased peak power capabilities compared to previous design approaches [6], [16], [53]. Specifically, during AB walking experiments, the prosthesis displayed peak joint powers of ~ 380 W, which is greater than the original design goal and ~ 200 and ~ 250 W peak power reported in [16] and [70], respectively. Furthermore, the peak power available to each actuator is more than 1 kW, which makes the leg suitable for more extreme tasks. Although the amputee subject exhibited similar pushoff powers at the fastest speed, a different walking style was adopted at slower speeds that resulted in lower pushoff powers than normal (see Fig. 22). It is likely that the TF subject's lack of experience with a powered leg contributed to consistently early transitions into swing when walking at slower speeds (see Fig. 21). Additional training and experience may be needed for the TF subject to leave the PR foot on the ground longer, therefore better utilizing the pushoff capabilities.

An interesting ancillary benefit of low-impedance actuators is similar to that of SEAs. Although the actuators implemented in the presented leg do not have an elastic element, they do have the ability to store energy. During phases of negative joint work, the generated energy can either be used within the leg's electrical system, to power the other joint, or to recharge the leg's batteries. This reduces power consumption and increases the efficiency of the PR leg for an extended battery life. Moreover, the low gear ratio reduces the amount of friction and reflected inertia that the motors have to overcome, thus further increasing the efficiency of the leg. To quantify this, a power analysis of the PR leg was conducted, which revealed a practical design advantage through a reduction in the average required power, compared to previous design approaches [6], [16]. During the TF walking trial, the prosthesis demonstrated an average specific power of 0.4 W/kg per gait cycle at very fast walking speeds (1.6 m/s), which is lower than 0.98 and 0.88 W/kg average seen in [16] and [70], respectively. Although we observed even lower specific powers at slower speeds, those cases are not used for comparison because of the lower pushoff powers observed. Nevertheless, the decreased power consumption allows the leg to take between 3263 and 14 875 PR steps on a single charge of the selected batteries. These values are more than sufficient for the daily use of an average TF amputee, who takes ~ 1540 PR steps per day [71]. Moreover, energy analysis shows that the

total mechanical energy is close to net-zero, similar to AB walking [39].

Very little is presented throughout the literature on the acoustic sound level of assistive devices [72] and powered PR legs [73]. The acoustic sound level becomes important to consider when attempting to translate this emerging technology to the consumer. Upon investigation, the PR leg with low-impedance actuators was on average 6 to 7 dB quieter than a PR leg with conventional actuation (see Fig. 20). In fact, peaks seen in the new actuator's sound level at the beginning of the gait cycle actually originate from impact with the ground, instead of the leg's actuators. Since control of foot planting was reduced when walking with a PR leg, which continues to decrease as speeds increase, the jump in sound is likely to be a result of the controller managing the leg at impacts. In comparison to typical household items, the sound level of the high-impedance PR leg is akin to a vacuum cleaner (6 to 70 dB at ~ 1.5 m), which is similar to the 70 dB (at ~ 1 m) presented in [73]. However, the low-impedance PR leg is akin to a refrigerator or an electric tooth brush (50 to 60 dB at ~ 1.5 m) [74]. Efforts can be made to further reduce the sound level of the prosthesis by enclosing or insulating the actuators, similar to commercial products.

B. Limitations

Concerning the design of the presented PR leg, its weight is the top limiting factor for clinical acceptance. A large portion of the leg's weight comes from the leg's structure and electric motors in the actuators. There is a tradeoff between an actuator's mass and its available power. For example, series elasticity could be used to lower the motor's power, therefore lowering the motor's mass. However, the addition of an elastic element (such as a spring) and other structural complexities would likely increase the total mass of the actuator. Low-impedance actuators avoid these components and will continue to get lighter as the torque and power density of motor technology improves over time.

An additional tradeoff is between the motor's mass and the actuator's backdrivability. Assuming the length of the motor is constant (which is typically determined by geometrical constraints), the following properties for scaling the motor in the radial direction hold [75]: motor torque $\tau_m \propto r_{\text{gap}}^2$, motor inertia $I_m \propto r_{\text{gap}}^3$, and motor mass $m_m \propto r_{\text{gap}}$, where r_{gap} is the distance from the axis of rotation to the center of the gap between the stator and rotor, or gap radius. Based on these relations, the gear ratio for a fixed joint torque $\tau_j = n\tau_m$ scales with $n \propto 1/r_{\text{gap}}^2$. Then, the reflected inertia at the joint will scale as $I_j = n^2 I_m \propto 1/r_{\text{gap}}$. Furthermore, increasing r_{gap} to achieve a lower reflected inertia typically results in a larger motor mass. On the other hand, the gear ratio is proportional to $1/r_{\text{gap}}^2$, which results in a smaller/lighter transmission with reduced friction [75].

Achieving low-impedance actuation resulted in a knee–ankle prosthesis with a mass of 6 kg, which is 1–2 kg heavier than some state-of-the-art knee–ankle prostheses [16], [25], [76]. Other recent works, such as the lightweight powered PR joints in [11],[20], and[24] have achieved a mass of 1–2 kg for a single actuated joint. Although the low-impedance actuation scheme

tends to be heavier than other powered prostheses, we believe the added mass is justified through the increased power and torque available to both joints, which produces larger pushoff and ground reaction forces. At the same time, the presented mass of 6 kg is much lighter than the 8.1 kg [77] and 11 kg [69] of other prostheses with similar power/torque ratings. Moreover, exploiting the proprioceptive characteristics of the actuator for detecting ground contact [34] could allow the removal of the load cell at the ankle, thus reducing the leg's mass by another 0.2 kg.

With the design of the leg now validated, additional amputee trials can be conducted to investigate clinical outcomes, such as the actuators' effect on gait compensations. Specifically, we expect that the increased torque bandwidth of the actuators will provide greater propulsion and toe clearance, thus reducing hip-hiking, vaulting, and circumduction. Optimizing these outcomes may require additional tuning to reduce the deviation of joint kinematics from normative patterns, which was larger than that reported with some other powered prostheses [18]. Tuning could also improve the pushoff output power at the cost of energy consumption. However, the various scenarios tested in this study suggest the leg will remain efficient as gait properties change.

VI. CONCLUSION

This article presented the design and experimental validation of a powered PR leg with high-torque, low-impedance actuators. The system implements high-torque motors coupled with low-reduction transmissions. Low mechanical impedance is an inherent feature of the actuators' design, resulting in low backdrive torques to move the motors.

Benchtop tests showed that the low-impedance actuators have negligible unmodeled actuator dynamics. This was further confirmed through the implementation of human walking impedances into an impedance-based walking controller, which demonstrated that accurate torque control is achievable without torque feedback. The low-impedance actuators were also able to maintain precise position tracking in both benchtop and walking experiments. The compliant nature of the prosthesis allowed for smooth transitions between the impedance- and position-based portions of the walking controller, such as the transition from high output torques at pushoff to high speeds at toe off. Furthermore, the low-impedance actuators presented practical advantages through reduced power consumption and acoustic sound levels.

Future work will include clinical testing with additional amputees to assess the effect the prosthesis has on gait compensations. Additional design revisions may be made to further simplify and reduce the weight and volume of the leg using light-weight materials, fewer sensors, and smaller electronics. Finally, this PR leg will be further used as a platform for control prototyping to advance the field of PR leg control.

APPENDIX A PARAMETER IDENTIFICATION

To identify the inertia and damping of the actuator, open-loop frequency response tests were performed with the knee actuator

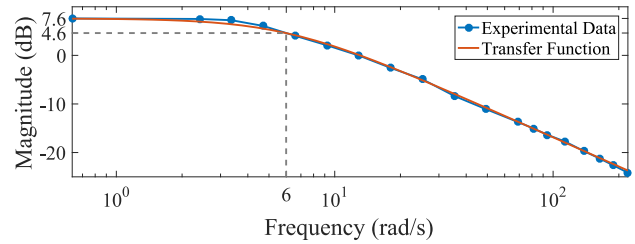


Fig. 23. Magnitude plot for open-loop frequency response tests. This displays the dc offset and cutoff frequency used to determine actuator impedance and damping.

fixed to the benchtop and disconnected from its output/load. Sinusoidal torque commands were directly sent to the motor driver and the actuator's velocity was recorded. The sinusoidal signal began at a very low frequency, and was incrementally increased to higher frequencies until the test had to be halted due to excessive shaking and vibrations, i.e., 0.1 to 35 Hz. The resulting magnitudes presented in Fig. 23 show a dc offset of 7.6 dB and a cutoff frequency of 6 rad/s at 4.6 dB (or -3 dB from dc offset). Assuming first-order dynamics of the form

$$G(s) = \frac{1}{Is + b} \quad (4)$$

the inertia I and damping b were identified as $0.0696 \text{ kg}\cdot\text{m}^2$ and $0.4169 \text{ N}\cdot\text{m}\cdot\text{s}/\text{rad}$, respectively. The frequency response of the system (4) with these values has been plotted over the experimental results in Fig. 23. The strong agreement between the two responses verifies that (4) closely explains the dynamics of the system.

APPENDIX B RANGE OF STABLE CONTROLLER GAINS FOR INTERACTION WITH A COMPLIANT ENVIRONMENT

Following Colgate and Schenkel [55] with the identified actuator parameters, the discrete-time stability margin for the controller can be obtained from the points at which the roots of the characteristic equation $1 + C(z)L^*(s)$ satisfy $|z| = 1$. Here, $C(z)$ is the discretized PD controller of (1), and $L^*(s)$ is the sampled-time version of $L(s)$, the transfer function of the actuator dynamics (4) interacting with the human's impedance $H(s)$

$$L(s) = \frac{1 - e^{-Ts}}{s^2} \frac{1}{Is + b + H(s)} \quad (5)$$

where T is the sampling time.

Although stability can be investigated for any passive $H(s)$ in (5), it will result in unnecessarily conservative limitations on the gains. As discussed in [55], considering the human impedance as a limited-stiffness spring provides a more realistic set of conditions for the interaction stability. Since the stiffnesses that human leg joints emulate are typically less than $3000 \text{ N}\cdot\text{m}/\text{rad}$ [78], [79], we performed the stability analysis with three different stiffness values: 100, 1000, and 10 000 $\text{N}\cdot\text{m}/\text{rad}$ to cover a range of compliant to rigid interactions. The stability margins are depicted in Fig. 24. The PD gains will be selected with regard to the obtained stable region.

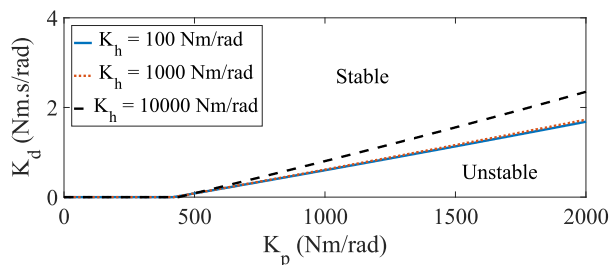


Fig. 24. Stability margins for three different human stiffness values, $K_h = 100, 1000,$ and $10\,000$ N-m/rad. The region above the margins is the stable region.

Note that the stable region obtained in Fig. 24 is still a conservative estimation. This is due to the fact that we did not consider the link inertias in our analysis to avoid nonlinearities, and as discussed in [55], the stable region grows with the increase in inertias. Moreover, we neglected interaction with the ground because the effective joint stiffness of PR feet is much smaller than $10\,000$ N-m/rad [80], and thus it does not affect our analysis.

ACKNOWLEDGMENT

The authors would like to thank Y. Chatzinoff, D. Merz, and K. Sheppard for assisting the mechanical design, and J. Doan, L. Zekarias, P. Krishnia, and H. Zhu for their programming and electrical assistance. The authors would also like to thank L. Gray for her assistance with the amputee experiment.

REFERENCES

- [1] W. Miller, A. Deathe, M. Speechley, and J. Koval, "The influence of falling, fear of falling, and balance confidence on prosthetic mobility and social activity among individuals with a lower extremity amputation," *Arch. Phys. Med. Rehabil.*, vol. 82, no. 9, pp. 1238–1244, 2001.
- [2] R. S. Gailey *et al.*, "Energy expenditure of trans-tibial amputees during ambulation at self-selected pace," *Prosthetics Orthotics Int.*, vol. 18, no. 2, pp. 84–91, 1994.
- [3] K. R. Kaufman, S. Frittoli, and C. A. Frigo, "Gait asymmetry of transfemoral amputees using mechanical and microprocessor-controlled prosthetic knees," *Clin. Biomech.*, vol. 27, no. 5, pp. 460–465, 2012.
- [4] B. G. Lambrecht and H. Kazerooni, "Design of a semi-active knee prosthesis," in *Proc. IEEE Int. Conf. Robot. Autom.*, 2009, pp. 639–645.
- [5] D. Berry, "Microprocessor prosthetic knees," *Phys. Med. Rehabil. Clin.*, vol. 17, no. 1, pp. 91–113, 2006.
- [6] D. S. Pieringer, M. Grimmer, M. F. Russold, and R. Rienner, "Review of the actuators of active knee prostheses and their target design outputs for activities of daily living," in *Proc. IEEE Int. Conf. Rehabil. Robot.*, 2017, pp. 1246–1253.
- [7] M. R. Tucker *et al.*, "Control strategies for active lower extremity prosthetics and orthotics: A review," *J. Neuroeng. Rehabil.*, vol. 12, no. 1, 2015.
- [8] M. Windrich, M. Grimmer, O. Christ, S. Rinderknecht, and P. Beckerle, "Active lower limb prosthetics: A systematic review of design issues and solutions," *Biomed. Eng. Online*, vol. 15, no. 3, 2016, Art. no. 140.
- [9] B. Laschowski and J. Andrysek, "Electromechanical design of robotic transfemoral prostheses," in *Proc. ASME Int. Des. Eng. Tech. Conf. Inf. Eng. Conf.*, 2018, Art. no. V05AT07A054.
- [10] T. Lenzi, J. Sensinger, J. Lipsey, L. Hargrove, and T. Kuiken, "Design and preliminary testing of the RIC hybrid knee prosthesis," in *Proc. IEEE Int. Conf. Eng. Med. Biol. Soc.*, 2015, pp. 1683–1686.
- [11] T. Lenzi, M. Cempini, L. Hargrove, and T. Kuiken, "Design, development, and validation of a lightweight non-backdrivable robotic ankle prosthesis," *IEEE/ASME Trans. Mechatronics*, vol. 24, no. 2, pp. 471–482, Apr. 2019.
- [12] A. Fu, C. Fu, K. Wang, D. Zhao, X. Chen, and K. Chen, "The key parameter selection in design of an active electrical transfemoral prosthesis," in *Proc. IEEE Int. Conf. Robot. Biomimetics*, 2013, pp. 1716–1721.
- [13] U.-J. Yang and J.-Y. Kim, "Mechanical design of powered prosthetic leg and walking pattern generation based on motion capture data," *Adv. Robot.*, vol. 29, no. 16, pp. 1061–1079, 2015.
- [14] D. Quintero, D. J. Villarreal, D. J. Lambert, S. Kapp, and R. D. Gregg, "Continuous-phase control of a powered knee-ankle prosthesis: Amputee experiments across speeds and inclines," *IEEE Trans. Robot.*, vol. 34, no. 3, pp. 686–701, Jun. 2018.
- [15] M. V. Pillai, H. Kazerooni, and A. Hurwicz, "Design of a semi-active knee-ankle prosthesis," in *Proc. IEEE Int. Conf. Robot. Autom.*, 2011, pp. 5293–5300.
- [16] B. E. Lawson, J. Mitchell, D. Truex, A. Shultz, E. Ledoux, and M. Goldfarb, "A robotic leg prosthesis: Design, control, and implementation," *IEEE Robot. Autom. Mag.*, vol. 21, no. 4, pp. 70–81, Dec. 2014.
- [17] S. K. Au and H. Herr, "Powered ankle-foot prosthesis," *IEEE Robot. Autom. Mag.*, vol. 15, no. 3, pp. 52–59, Sep. 2008.
- [18] F. Sup, A. Bohara, and M. Goldfarb, "Design and control of a powered transfemoral prosthesis," *Int. J. Robot. Res.*, vol. 27, no. 2, pp. 263–273, 2008.
- [19] C. D. Hoover, G. D. Fulk, and K. B. Fite, "The design and initial experimental validation of an active myoelectric transfemoral prosthesis," *J. Med. Devices*, vol. 6, no. 1, 2012, Art. no. 011005.
- [20] T. Lenzi, M. Cempini, L. Hargrove, and T. Kuiken, "Design, development, and testing of a lightweight hybrid robotic knee prosthesis," *Int. J. Robot. Res.*, vol. 37, no. 8, pp. 953–976, 2018.
- [21] R. Borjjan, J. Lim, M. B. Khamesee, and W. Melek, "The design of an intelligent mechanical active prosthetic knee," in *Proc. IEEE Conf. Ind. Electron.*, 2008, pp. 3016–3021.
- [22] A. O. Kapti and M. S. Yucenur, "Design and control of an active artificial knee joint," *Mechanism Mach. Theory*, vol. 41, no. 12, pp. 1477–1485, 2006.
- [23] M. Liu, P. Datsis, and H. H. Huang, "A prototype for smart prosthetic legs—analysis and mechanical design," *Adv. Mater. Res.*, vol. 403, pp. 1999–2006, 2012.
- [24] M. Tran, L. Gabert, M. Cempini, and T. Lenzi, "A lightweight, efficient fully-powered knee prosthesis with actively variable transmission," *IEEE Robot. Autom. Lett.*, vol. 4, no. 2, pp. 1186–1193, Apr. 2019.
- [25] A. F. Azocar, L. M. Mooney, L. J. Hargrove, and E. J. Rouse, "Design and characterization of an open-source robotic leg prosthesis," in *Proc. IEEE Int. Conf. Biomed. Robot. Biomechanics*, 2018, pp. 111–118.
- [26] S. Seok *et al.*, "Design principles for energy-efficient legged locomotion and implementation on the MIT Cheetah robot," *IEEE/ASME Trans. Mechatronics*, vol. 20, no. 3, pp. 1117–1129, Jun. 2015.
- [27] T. Apgar, P. Clary, K. Green, A. Fern, and J. Hurst, "Fast online trajectory optimization for the bipedal robot Cassie," in *Proc. Robot.: Sci. Syst.*, 2018.
- [28] G. Kenneally, A. De, and D. E. Koditschek, "Design principles for a family of direct-drive legged robots," *IEEE Robot. Autom. Lett.*, vol. 1, no. 2, pp. 900–907, Jul. 2016.
- [29] J. Ramos, B. Katz, M. Y. M. Chuah, and S. Kim, "Facilitating model-based control through software-hardware co-design," in *Proc. IEEE Int. Conf. Robot. Autom.*, 2018, pp. 566–572.
- [30] G. Lv, H. Zhu, and R. Gregg, "On the design and control of highly backdrivable lower-limb exoskeletons," *IEEE Control Syst. Mag.*, vol. 38, no. 6, pp. 88–113, Dec. 2018.
- [31] H. Zhu, C. Nesler, N. Divekar, M. T. Ahmad, and R. D. Gregg, "Design and validation of a partial-assist knee orthosis with compact, backdrivable actuation," in *Proc. IEEE Int. Conf. Rehabil. Robot.*, 2019, pp. 917–924.
- [32] J. Wang *et al.*, "Comfort-centered design of a lightweight and backdrivable knee exoskeleton," *IEEE Robot. Autom. Lett.*, vol. 3, no. 4, pp. 4265–4272, Oct. 2018.
- [33] N. Paine, S. Oh, and L. Sentis, "Design and control considerations for high-performance series elastic actuators," *IEEE/ASME Trans. Mechatronics*, vol. 19, no. 3, pp. 1080–1091, Jun. 2014.
- [34] P. M. Wensing, A. Wang, S. Seok, D. Otten, J. Lang, and S. Kim, "Proprioceptive actuator design in the MIT Cheetah: Impact mitigation and high-bandwidth physical interaction for dynamic legged robots," *IEEE Trans. Robot.*, vol. 33, no. 3, pp. 509–522, Jun. 2017.
- [35] A. M. Simon *et al.*, "Configuring a powered knee and ankle prosthesis for transfemoral amputees within five specific ambulation modes," *PLoS ONE*, vol. 9, no. 6, 2014, Art. no. e99387.
- [36] J. W. Sensinger and J. H. Lipsey, "Cycloid vs. harmonic drives for use in high ratio, single stage robotic transmissions," in *Proc. IEEE Int. Conf. Robot. Autom.*, 2012, pp. 4130–4135.

- [37] Z. Levai, "Structure and analysis of planetary gear trains," *J. Mechanisms*, vol. 3, no. 3, pp. 131–148, 1968.
- [38] T. Elery, S. Rezaadeh, C. Nesler, J. Doan, H. Zhu, and R. D. Gregg, "Design and benchtop validation of a powered knee-ankle prosthesis with high-torque, low-impedance actuators," in *Proc. IEEE Int. Conf. Robot. Autom.*, 2018, pp. 2788–2795.
- [39] D. A. Winter, *Biomechanics and Motor Control of Human Movement*, 2nd ed. New York, NY, USA: Wiley, 2009.
- [40] K. R. Embry, D. J. Villarreal, and R. D. Gregg, "A unified parameterization of human gait across ambulation modes," in *Proc. IEEE Eng. Med. Biol. Conf.*, 2016, pp. 2179–2183.
- [41] E. D. Ledoux and M. Goldfarb, "Control and evaluation of a powered transfemoral prosthesis for stair ascent," *IEEE Trans. Neural Syst. Rehabil. Eng.*, vol. 25, no. 7, pp. 917–924, Jul. 2017.
- [42] B. Lawson, H. Varol, A. Huff, E. Erdemir, and M. Goldfarb, "Control of stair ascent and descent with a powered transfemoral prosthesis," *IEEE Trans. Neural Syst. Rehabil. Eng.*, vol. 21, no. 3, pp. 466–473, May 2013.
- [43] M. A. McDowell, C. D. Fryar, C. L. Ogden, and K. M. Flegal, "Anthropometric reference data for children and adults: United states, 2003–2006," *Nat. Health Statist. Rep.*, vol. 10, pp. 1–48, 2008.
- [44] V. Gupta and A. Deb, "Analysis of variable gear system on energy consumption in electric vehicle using simulation tool," *Int. J. Simul. Syst., Sci. Technol.*, vol. 13, no. 2, pp. 7–11, 2012.
- [45] Y. Ding and H. W. Park, "Design and experimental implementation of a quasi-direct-drive leg for optimized jumping," in *Proc. IEEE/RSJ Int. Conf. Intell. Robots Syst.*, 2017, pp. 300–305.
- [46] G. L. Smidt, "Biomechanical analysis of knee flexion and extension," *J. Biomechanics*, vol. 6, no. 1, pp. 79–80, 1973.
- [47] S. Pfeifer, R. Riener, and H. Vallery, "An actuated transfemoral prosthesis with optimized polycentric knee joint," in *Proc. IEEE Int. Conf. Biomed. Robot. Biomechatronics*, 2012, pp. 1807–1812.
- [48] Census.gov, "Table 205. Cumulative percent distribution of population by height and sex: 2007 to 2008," 2011. [Online]. Available: <https://www2.census.gov/library/publications/2010/compendia/statab/130ed/tables/11s0205.pdf>
- [49] R. C. Browning, J. R. Modica, R. Kram, and A. Goswami, "The effects of adding mass to the legs on the energetics and biomechanics of walking," *Med. Sci. Sports Exercise*, vol. 39, no. 3, pp. 515–525, 2007.
- [50] M. Cempini, L. J. Hargrove, and T. Lenzi, "Design, development, and bench-top testing of a powered polycentric ankle prosthesis," in *Proc. IEEE/RSJ Int. Conf. Intell. Robots Syst.*, 2017, pp. 1064–1069.
- [51] A. K. LaPre and F. Sup, "Redefining prosthetic ankle mechanics: Non-anthropomorphic ankle design," in *Proc. IEEE Int. Conf. Rehabil. Robot.*, 2013, pp. 1–5.
- [52] R. D. Gregg, T. Lenzi, L. J. Hargrove, and J. W. Sensinger, "Virtual constraint control of a powered prosthetic leg: From simulation to experiments with transfemoral amputees," *IEEE Trans. Robot.*, vol. 30, no. 6, pp. 1455–1471, Dec. 2014.
- [53] S. Rezaadeh, D. Quintero, N. Divekar, and R. D. Gregg, "A phase variable approach to volitional control of powered knee-ankle prostheses," in *Proc. IEEE/RSJ Int. Conf. Intell. Robots Syst.*, Madrid, Spain, 2018, pp. 2292–2298.
- [54] N. Hogan, "Impedance control: An approach to manipulation: Part II-Implementation," *J. Dyn. Syst., Meas., Control*, vol. 107, no. 1, pp. 8–16, 1985.
- [55] J. E. Colgate and G. G. Schenkel, "Passivity of a class of sampled-data systems: Application to haptic interfaces," *J. Robot. Syst.*, vol. 14, no. 1, pp. 37–47, 1997.
- [56] D. L. Jindrich and R. J. Full, "Dynamic stabilization of rapid hexapedal locomotion," *J. Exp. Biol.*, vol. 205, no. 18, pp. 2803–2823, 2002.
- [57] U. Saranlı, M. Buehler, and D. E. Koditschek, "RHex: A simple and highly mobile hexapod robot," *Int. J. Robot. Res.*, vol. 20, no. 7, pp. 616–631, 2001.
- [58] S. Rezaadeh, A. Abate, R. L. Hatton, and J. W. Hurst, "Robot leg design: A constructive framework," *IEEE Access*, vol. 6, no. 1, pp. 54369–54387, 2018.
- [59] S. Rezaadeh *et al.*, "Spring-mass walking with ATRIAS in 3D: Robust gait control spanning zero to 4.3 KPH on a heavily underactuated bipedal robot," in *Proc. ASME Dyn. Syst. Control Conf.*, 2015, Art. no. V001T04A003.
- [60] M. Eilenberg, H. Geyer, and H. Herr, "Control of a powered ankle-foot prosthesis based on a neuromuscular model," *IEEE Trans. Neural Syst. Rehabil. Eng.*, vol. 18, no. 2, pp. 164–173, Apr. 2010.
- [61] A. H. Shultz, B. E. Lawson, and M. Goldfarb, "Variable cadence walking and ground adaptive standing with a powered ankle prosthesis," *IEEE Trans. Neural Syst. Rehabil. Eng.*, vol. 24, no. 4, pp. 495–505, Apr. 2016.
- [62] K. Shamaei, G. S. Sawicki, and A. M. Dollar, "Estimation of quasi-stiffness of the human knee in the stance phase of walking," *PLoS ONE*, vol. 8, no. 3, 2013, Art. no. e59993.
- [63] K. Shamaei, G. S. Sawicki, and A. M. Dollar, "Estimation of quasi-stiffness and propulsive work of the human ankle in the stance phase of walking," *PLoS ONE*, vol. 8, no. 3, 2013, Art. no. e59935.
- [64] T. Lenzi, L. Hargrove, and J. Sensinger, "Speed-adaptation mechanism: Robotic prostheses can actively regulate joint torque," *IEEE Robot. Autom. Mag.*, vol. 21, no. 4, pp. 94–107, Dec. 2014.
- [65] A. Martin and R. D. Gregg, "Stable, robust hybrid zero dynamics control of powered lower-limb prostheses," *IEEE Trans. Autom. Control*, vol. 62, no. 8, pp. 3930–3942, Aug. 2017.
- [66] D. Satkunskienė, V. Grigas, V. Eidukynas, and A. Domeika, "Acceleration based evaluation of the human walking and running parameters," *J. Vibroeng.*, vol. 11, no. 1, pp. 506–510, 2009.
- [67] D. Quintero, D. J. Villarreal, and R. D. Gregg, "Preliminary experimental results of a unified controller for a powered knee-ankle prosthetic leg over various walking speeds," in *Proc. IEEE Int. Conf. Intell. Robots Syst.*, 2016, pp. 5427–5433.
- [68] H. Zhao, J. Reher, J. Horn, V. Paredes, and A. D. Ames, "Realization of nonlinear real-time optimization based controllers on self-contained transfemoral prosthesis," in *Proc. ACM/IEEE Conf. Cyber-Phys. Syst.*, 2015, pp. 130–138.
- [69] N. Thatte and H. Geyer, "Toward balance recovery with leg prostheses using neuromuscular model control," *IEEE Trans. Biomed. Eng.*, vol. 63, no. 5, pp. 904–913, May 2016.
- [70] F. Sup, H. A. Varol, J. Mitchell, T. J. Withrow, and M. Goldfarb, "Preliminary evaluations of a self-contained anthropomorphic transfemoral prosthesis," *IEEE/ASME Trans. Mechatronics*, vol. 14, no. 6, pp. 667–676, Dec. 2009.
- [71] E. G. Halsne, M. G. Waddingham, and B. J. Hafner, "Long-term activity in and among persons with transfemoral amputation," *J. Rehabil. Res. Develop.*, vol. 50, no. 4, pp. 515–530, 2013.
- [72] R. J. Farris, H. A. Quintero, and M. Goldfarb, "Preliminary evaluation of a powered lower limb orthosis to aid walking in paraplegic individuals," *IEEE Trans. Neural Syst. Rehabil. Eng.*, vol. 19, no. 6, pp. 652–659, Dec. 2011.
- [73] F. C. Sup IV, "A powered self-contained knee and ankle prosthesis for near normal gait in transfemoral amputees," Ph.D. dissertation, Dept. Mech. Eng., Vanderbilt Univ., Nashville, TN, USA, 2009.
- [74] R. L. C. Company, "dBA comparisons," 2012. [Online]. Available: <https://www.rlcraigco.com/pdf/dba-comparison.pdf>
- [75] S. Seok, A. Wang, D. Otten, and S. Kim, "Actuator design for high force proprioceptive control in fast legged locomotion," in *Proc. IEEE/RSJ Int. Conf. Intell. Robots Syst.*, 2012, pp. 1970–1975.
- [76] E. J. Rouse, L. M. Mooney, and H. M. Herr, "Clutchable series-elastic actuator: Implications for prosthetic knee design," *Int. J. Robot. Res.*, vol. 33, no. 13, pp. 1611–1625, 2014.
- [77] J. C. Horn, "Design and implementation of the powered self-contained AMPRO prostheses," Master's thesis, Dept. Mech. Eng., Texas A&M Univ., College Station, TX, USA, 2015.
- [78] C. T. Farley, H. H. Houdijk, C. Van Strien, and M. Louie, "Mechanism of leg stiffness adjustment for hopping on surfaces of different stiffnesses," *J. Appl. Physiol.*, vol. 85, no. 3, pp. 1044–1055, 1998.
- [79] S. Kuitunen, K. Ogiso, and P. Komi, "Leg and joint stiffness in human hopping," *Scand. J. Med. Sci. Sports*, vol. 21, no. 6, pp. e159–e167, 2011.
- [80] P. G. Adamczyk, M. Roland, and M. E. Hahn, "Novel method to evaluate angular stiffness of prosthetic feet from linear compression tests," *J. Biomech. Eng.*, vol. 135, no. 10, 2013, Art. no. 104502.



Toby Elery (Student Member, IEEE) received the B.S., M.S., and Ph.D. degrees in mechanical engineering from The University of Texas at Dallas, Richardson, TX, USA, in 2014, 2017, and 2020, respectively.

He is currently a Postdoctoral Researcher with The University of Texas at Dallas. His research interests include design innovation for powered prosthetic legs, orthoses, exoskeletons, and assistive devices.



Siavash Rezazadeh (Member, IEEE) received the B.S. and M.S. degrees in mechanical engineering from the Sharif University of Technology, Tehran, Iran, in 2001 and 2004, and the Ph.D. degree in mechanical engineering from the University of Alberta, Edmonton, AB, Canada, in 2012.

He is currently an Assistant Professor with the Department of Mechanical and Materials Engineering, University of Denver, Denver, CO, USA. Prior to this, he was a Research Scientist with the Locomotor Control Systems Laboratory, The University of Texas at Dallas, Richardson, TX, USA, working on design and control of prosthetic legs. Between 2012 and 2015, he was a Postdoctoral Researcher with the Dynamic Robotics Laboratory, Oregon State University, Corvallis, OR, USA, on control of ATRIAS, a bipedal robot, for DARPA Robotics Challenge. His research interest includes using fundamental concepts of mechanics for design and control of novel robots and mechanisms.



Robert D. Gregg (Senior Member, IEEE) received the B.S. degree in electrical engineering and computer sciences from the University of California at Berkeley, Berkeley, CA, USA, in 2006, and the M.S. and Ph.D. degrees in electrical and computer engineering from the University of Illinois at Urbana–Champaign, Champaign, IL, USA, in 2007 and 2010, respectively.

He joined the Department of Electrical Engineering and Computer Science, Robotics Institute, University of Michigan (UM), Ann Arbor, MI, USA, as an Associate Professor, in fall 2019. Prior to joining UM, he was an Assistant Professor with the Department of Bioengineering and Mechanical Engineering, The University of Texas at Dallas, Richardson, TX, USA. He was also a Research Scientist with the Rehabilitation Institute of Chicago, Chicago, IL, USA, and a Postdoctoral Fellow with the Northwestern University, Evanston, IL, USA. His research interest includes control of bipedal locomotion with applications to autonomous and wearable robots.



Christopher Nesler received the B.S. degree in mechanical engineering from Oregon State University, Corvallis, OR, USA, in 2014, and the M.S. degree in biomedical engineering from the Northwestern University, Evanston, IL, USA, in 2016.

He is currently a Research Engineer with the Locomotor Control Systems Laboratory, University of Michigan (The University of Texas at Dallas), Ann Arbor, MI, USA, where he works on design and improvement of various powered lower limb prostheses and exoskeletons.